



This work is licensed under the Creative Commons Attribution-NonCommercial-NoDerivatives 4.0 International License. To view a copy of this license, visit <http://creativecommons.org/licenses/by-nc-nd/4.0/> or send a letter to Creative Commons, PO Box 1866, Mountain View, CA 94042, USA.

Flood propagation modelling with the Local Inertia Approximation: theoretical and numerical analysis

Luca Cozzolino¹, Luigi Cimorelli², Renata Della Morte³, Giovanni Pugliano⁴, Vincenzo Piscopo⁵, Domenico Pianese⁶

Abstract

Attention of the researchers has increased towards a simplification of the complete Shallow water Equations called the Local Inertia Approximation (LInA), which is obtained by neglecting the advection term in the momentum conservation equation. This model is commonly used for the simulation of slow flooding phenomena characterized by small velocities and absence of flow discontinuities. In the present paper it is demonstrated that discontinuities are always developed at moving wetting-drying frontiers, and this justifies the study of the Riemann problem on even and uneven beds. In particular, the general exact solution for the Riemann problem on horizontal frictionless bed is given, together with the exact solution of the non-breaking wave propagating on

¹ Sen. Res., Ph. D., Dept. of Engrg., Parthenope Univ., Centro Direzionale di Napoli – Is. C4, 80143 Napoli, Italy. E-mail: luca.cozzolino@uniparthenope.it

² Sen. Res., Ph. D., Dept. of Civil, Architectural and Environmental Engrg., Federico II Univ., via Claudio 21, 80125 Napoli, Italy. E-mail: luigi.cimorelli@unina.it

³ Full Prof., Ph. D., Dept. of Engrg., Parthenope Univ., Centro Direzionale di Napoli – Is. C4, 80143 Napoli, Italy. E-mail: renata.dellamorte@uniparthenope.it

⁴ Ass. Prof., Ph. D., Dept. of Engrg., Parthenope Univ., Centro Direzionale di Napoli – Is. C4, 80143 Napoli, Italy. E-mail: giovanni.pugliano@uniparthenope.it

⁵ Jun. Res., Ph. D., Dept. of Sci. and Tech., Parthenope Univ., Centro Direzionale di Napoli – Is. C4, 80143 Napoli, Italy. E-mail: vincenzo.piscopo@uniparthenope.it

⁶ Full Prof., Dept. of Civil, Architectural and Environmental Engrg., Federico II Univ., via Claudio 21, 80125 Napoli, Italy. E-mail: pianese@unina.it

horizontal bed with friction, while some example solution is given for the Riemann problem on discontinuous bed. From this analysis, it follows that drying of the wet bed is forbidden in the LInA model, and that there are initial conditions for which the LInA has no solution. In addition, the numerical analysis has confirmed that non-conservative schemes cannot be used for the propagation of the LInA on dry bed, because they converge to a wrong solution. Following the preceding results, two new criteria for the definition of the applicability limits of the LInA model have been proposed, based respectively on the limitation of the wetting front velocity and the limitation of spurious total head variations.

Keywords: Shallow-water Equations; Local Inertia Approximation; Riemann problem; Flooding; Exact solution; Numerical solution.

E-mail address: luca.cozzolino@uniparthenope.it

Address: Dipartimento di Ingegneria, Università degli Studi di Napoli Parthenope, Isola C4, 80143 Napoli (Italy)

Phone: +390815476723.

1 Introduction

It is well recognized that flooding risk is now a global issue, with more than $2.8 \cdot 10^9$ people affected in the years from 1980 to 2009 (Doocy et al. 2013). There is statistical evidence that the climate change is driving the increase of heavy precipitation events (Kundzewich et al. 2014), leading to an increase of the flooding hazard. On the other side, flood risk is becoming an issue in urban areas, due to the rapid growing of population in the cities and the steady anthropic pressure on the environment (Chen et al. 2015). These observations highlight the need of implementing robust and physically based models for the evaluation of flooded area extents, and for the evaluation of countermeasures efficiency.

The Shallow water Equations (SWE) are the elective mathematical model for the computation of flood propagation in floodplains (Liang et a. 2008), urban flooding (Mignot et al. 2006), tsunami propagation in coastal areas (LeVeque et al. 2011), and dam-break computation (Wang et al. 2011). This versatility of use is justified by the ability of the SWE to cope with real-flow physical features such as supercritical, subcritical, as well as transcritical flow conditions. In addition, the SWE can manage with moving flow field discontinuities (Montuori and Greco 1973), discontinuous geometries (Alcrudo and Benkhaldoun 2001, Cozzolino et al. 2017), and wetting-drying fronts (Sobey 2009). The two dimensional SWE satisfy the rotation invariance property (Toro 2001), and for this reason the one-dimensional SWE model

$$(1) \quad \begin{aligned} \frac{\partial h}{\partial t} + \frac{\partial hu}{\partial x} &= 0 \\ \frac{\partial hu}{\partial t} + \frac{\partial}{\partial x} \left(\frac{gh^2}{2} + hu^2 \right) &= -gh \frac{\partial z}{\partial x} - ghS_f \end{aligned}$$

is sufficient to study the essential characteristics of the mathematical model. In Eq. (1), the symbols have the following meaning: x and t are the space and time independent variables, respectively; $h(x,$

t) is the flow depth, while $u(x, t)$ is the vertically averaged flow velocity; $g = 9.81 \text{ m}^2/\text{s}$ is the gravity acceleration; $z(x)$ is the bed elevation; and $S_f = S_f(x, h, u)$ is the friction slope. The first of Eq. (1) represents the differential form of the mass conservation principle, while the second equation represents the second principle of the dynamics (often called momentum conservation equation). The solutions of Eq. (1) must be characterised by the flow depth-positivity property, namely the condition $h > 0$ must be satisfied.

Computation of flooding with the SWE is based on a delicate equilibrium between the need of a complete physical representation and the need for fast computation. These two competing objectives cannot be simultaneously fulfilled, because more physically accurate models lead to an increased amount of calculations. Numerical issues have been reported for finite-difference schemes written in non-conservative form when flow field discontinuities are present (Hou and LeFloch 1994), and conservative schemes (Aldrichetti and Zanolli 2005) may be preferred in this case; nonetheless, this introduces the need of adopting special time-consuming procedures of balancing between fluxes and source terms when high-order accuracy is required (Xing and Shu 2005).

Numerical problems at the wetting-drying front are present also when propagating bores are absent, and this has been attributed to the presence of the advection terms in the SWE (Natale and Savi 1991, Galbiati and Savi 1995, Aronica et al. 1998, Bates et al 2010). These issues may be circumvented by adopting very small space and time steps during computations (Burguete et al. 2007), but this procedure inevitably increases the computational burden. For this reason, alternative strategies must be devised in order to ensure fast calculations.

Recently, attention of the researchers has increased towards a simplification of the complete SWE called the Local Inertia Approximation (LInA). This system of equations, whose one-dimensional version is

$$(2) \quad \begin{aligned} \frac{\partial h}{\partial t} + \frac{\partial hu}{\partial x} &= 0 \\ \frac{\partial hu}{\partial t} + \frac{\partial}{\partial x} \frac{gh^2}{2} &= -gh \frac{\partial z}{\partial x} - ghS_f \end{aligned}$$

is obtained by neglecting the advection term in the momentum conservation equation of the SWE, while retaining the local inertial term. The LInA is a non-linear system of hyperbolic differential equations (Natale and Savi 1991) that has been first used in oceanography (Uusitalo 1960, Sielecki 1963) for storm-surge computation in sea basins with fixed wet-dry boundaries. Successively, its use has been extended to border irrigation computation (Natale and Savi 1991, Galbiati and Savi 1995), and wave propagation on floodplains (Aronica et al. 1998, Moramarco et al. 2005). The system of Eq. (2) is now an active field of study, with flood propagation applications at urban (Neal et al. 2011, Martins et al. 2016c, Martins et al. 2017), basin (Coulthard et al. 2013, Savage et al. 2016, Nguyen et al. 2016), and regional scale (Falter et al. 2013, Yamazaki et al. 2013, Mateo et al. 2017).

The theoretical study on flooding applications with LInA model has begun with the work by Bates et al. (2010). In that paper, it was shown that the LInA is a viable alternative to the complete model when bed roughness is not low. Neal et al. (2012) reported that the lack of the advection term in the momentum equation prevented the model from correctly representing the regions of the flow field characterized by critical or transcritical flow. de Almeida and Bates (2013) showed with steady flow numerical experiments that the LInA is an accurate approximation of the SWE for subcritical flows with Froude number less than 0.5, and with Froude numbers in the range [0.5, 1] and mild flow depth gradients. In addition, they found numerically that the LInA systematically underestimates the wave front speed in flooding experiments. Martins et al. (2016b) supplied the exact solution of the dam-break for the LInA, and compared it with the corresponding solution of the SWE, showing that the LInA fails in reproducing supercritical flows.

The theoretical study of the LInA has been accompanied by the development of numerical models for the approximation of its solution. Bates et al. (2010) demonstrated that a simple raster-based explicit LInA numerical model exhibited a reduced computational burden with respect to a similar numerical implementation of the diffusive wave (Hunter et al. 2005). This result was successively confirmed by Dottori and Todini (2011) and Neal et al. (2011). The maximum time step was evaluated by Bates et al. (2010) on the basis of linear stability considerations, taking into account the flow depth and discarding the flow velocity, but no theoretical justification was given. Neal et al. (2012) reported that an explicit raster-based implementation of the LInA exhibited significant total conserved mass error, together with numerical instabilities at the wetting front when the values of the bed roughness were low. In order to improve the stability of the model, de Almeida et al. (2012) proposed a numerical scheme (termed *q-centered* scheme) with semi-implicit treatment of the friction source term and discretisation of the momentum equation inspired by the Lax-Friedrichs model. Martins et al. (2015) presented a Finite Volume scheme equipped with the approximate Roe solver for the computation of fluxes between cells. In the same paper, it was given a novel stability condition where both flow depth and velocity were taken into account, but again no theoretical justification was given. In Martins et al. (2016a), a Finite Volume scheme based on the Roe Riemann solver and a MacCormack finite difference scheme were tested using the dam-break exact solution. The results showed that numerical algorithms written in conservative form are able to reproduce moving discontinuities arising in LInA. Finally, numerous empirical methods for the treatment of wetting-drying problems were compared in Martins et al. (2018), but none of these methods was based on the definition of a theoretical maximum time step.

As a result of the theoretical analyses available in the literature (Neal et al. 2012, de Almeida and Bates 2013), it is commonly understood that the LInA model “should only be applied in sub-critical flow conditions and with gradually varying flow” (Coulthard et al. 2013). This has justified the use of the LInA for the simulation of slow flooding phenomena characterized by small velocities and absence of flow discontinuities. Nonetheless, in the second Section of the present

paper it will be demonstrated that the wet-dry frontiers with null flow depth are always at rest in the LInA model, and this implies that discontinuities must develop at moving wetting-drying frontiers in problems of practical interest. This surprising result motivates the general study of moving discontinuities for flooded area calculation with LInA. This study can be exhaustively conducted in the context of the Riemann problem for the LInA model, and it is precisely the subject of the present work.

The paper is organized as follows. In the second Section, it is shown that the free surface profile can be continuously connected to the dry bed in the case of wet-dry frontier at rest only. An interesting consequence of this result is that moving frontiers between wet and dry bed are always shocks. In the third Section, the complete solution of the Riemann problem on horizontal frictionless bed is supplied, with special attention to the Riemann problem on dry bed. The characterization of the moving discontinuities on the dry bed allows finding a second surprising result, namely that the LInA model supports only wetting phenomena, while authentic drying phenomena are forbidden. In the fourth Section, the exact solution of the non-breaking wave on horizontal bed with friction is given, showing that the flooding wave is led by a shock that satisfies the theoretical treatment of the preceding section. Irregularities of the bed elevation and obstacles are commonly present in the flooded areas, and the interaction of moving flow discontinuities with these geometrical singularities is tackled in the context of the Riemann problem with discontinuous bed elevation in the fifth Section. In the sixth Section, a widely used numerical model (de Almeida et al. 2012) is studied with reference to its flow propagation properties, in light of the theoretical results presented in the preceding sections. The consequences of these results are discussed in the seventh Section, while Conclusions are draft in the final Section.

2 Wetting-drying frontier in the LInA

The preliminary study of the wetting-drying frontier can be conducted in the context of the classic method of characteristics for hyperbolic systems of differential equations (Abbott 1966). The trajectory of this front is $x_F = x_F(t)$, while the corresponding velocity $dx_F(t)/dt = u(x_F(t), t)$ coincides with the local flow velocity (Sobey 2009). This implies that $h(x_F(t), t) = 0$ in the case that the flow is continuously connected to the dry bed. If discontinuities are absent, some working shows that Eq. (2) can be rewritten in the following form (compare with the corresponding expression in Martins et al. 2016a,b)

$$(3) \quad \begin{aligned} \frac{\partial I_1(\mathbf{u})}{\partial t} + \lambda_1(\mathbf{u}) \frac{\partial I_1(\mathbf{u})}{\partial x} &= -gh \frac{\partial z}{\partial x} - ghS_f, \\ \frac{\partial I_2(\mathbf{u})}{\partial t} + \lambda_2(\mathbf{u}) \frac{\partial I_2(\mathbf{u})}{\partial x} &= -gh \frac{\partial z}{\partial x} - ghS_f, \end{aligned}$$

where $\mathbf{u}(x, t) = (h \quad hu)^T$ is the vector of the conserved variables, T is the symbol of matrix transpose, $\lambda_1(\mathbf{u})$ and $\lambda_2(\mathbf{u})$ are defined as

$$(4) \quad \lambda_1(\mathbf{u}) = -\sqrt{gh}, \quad \lambda_2(\mathbf{u}) = \sqrt{gh},$$

while $I_1(\mathbf{u})$ and $I_2(\mathbf{u})$ are defined as

$$(5) \quad I_1(\mathbf{u}) = hu - \frac{2}{3}h\sqrt{gh}, \quad I_2(\mathbf{u}) = hu + \frac{2}{3}h\sqrt{gh}.$$

It is possible to demonstrate the following

Proposition 1. *The free surface profile can be continuously connected to the dry bed only in the case of wet-dry frontier at rest.*

Proof. The Eq. (3) can be interpreted in the sense that the information about the flow is transported by I_1 and I_2 along the characteristic curves of the plane (x, t) defined by $dx/dt = \lambda_1$ and $dx/dt = \lambda_2$, respectively. The celerities λ_1 and λ_2 are null at the wetting-drying frontier with $h \rightarrow 0$, and this implies that the information originating from x_F cannot propagate. In other words, the wet-dry frontier with null flow-depth cannot move.

By exclusion, an immediate consequence of Proposition 1 is a surprising result that is formulated here for the first time, namely that moving frontiers compatible with the LInA model can be shocks only. The Proposition 1 highlights the importance of studying moving discontinuities in the LInA model, and this can be accurately accomplished in the context of the Riemann problem solution.

3 Solution of the Riemann problem on horizontal bed without friction

In the present section, the general solution of the Riemann problem for the LInA model is discussed, and its results are compared with those supplied by the SWE (whose complete solution can be found in Toro 2001). Special attention is given to the Riemann problem on dry bed.

3.1 Position of the Riemann problem and general solution

If the bed is horizontal and frictionless, the Eq. (2) can be rewritten as

$$(6) \frac{\partial \mathbf{u}}{\partial t} + \frac{\partial \mathbf{f}(\mathbf{u})}{\partial x} = 0,$$

where $\mathbf{f}(\mathbf{u}) = (hu \quad 0.5gh^2)^T$ is the vector of the fluxes. The eigenvalues $\lambda_1(\mathbf{u})$ and $\lambda_2(\mathbf{u})$ of the Jacobian matrix $\mathbf{A}(\mathbf{u}) = \partial \mathbf{f} / \partial \mathbf{u}$ are defined by Eq. (4), with corresponding eigenvectors (de Almeida et al. 2012, Yamazaki et al. 2015)

$$(7) \mathbf{r}_1(\mathbf{u}) = (1 \quad -\sqrt{gh})^T, \quad \mathbf{r}_2(\mathbf{u}) = (1 \quad \sqrt{gh})^T.$$

The eigenvectors $\mathbf{r}_1(\mathbf{u})$ and $\mathbf{r}_2(\mathbf{u})$ are real valued and linearly independent for each $h > 0$, and this implies that the system of Eq. (6) is strictly hyperbolic. It is easy to see (Appendix A) that the first and the second characteristic field are genuinely non-linear, and that they may contain either rarefactions or shock waves.

The Riemann problem consists in solving the system of Eq. (6) with the following discontinuous initial conditions:

$$(8) \mathbf{u}(x,0) = \begin{cases} x < 0, & \mathbf{u}_L = (h_L \quad h_L u_L)^T \\ x > 0, & \mathbf{u}_R = (h_R \quad h_R u_R)^T \end{cases}.$$

The solution of the Riemann problem is self-similar, and then a vector function $\mathbf{v}(s)$ of the scalar parameter s exists such as $\mathbf{u}(x,t) = \mathbf{v}(x/t)$. For $t > 0$, the initial left state \mathbf{u}_L and the initial right state \mathbf{u}_R are separated by the intermediate state $\mathbf{u}_M = (h_M \quad h_M u_M)^T$, which is in turn connected to \mathbf{u}_L by means of a wave (a shock or a rarefaction) contained in the first characteristic field, and it is connected to \mathbf{u}_R by a wave (a shock or a rarefaction) contained into the second characteristic field.

3.1.1 Elementary waves

In the plane (h, hu) , the direct 1-wave curve

$$(9) \quad H_1(\mathbf{u}, \mathbf{u}_0) = \begin{cases} R_1(\mathbf{u}, \mathbf{u}_0): & 0 < h \leq h_0, \quad hu = h_0 u_0 + 2(h_0 \sqrt{gh_0} - h \sqrt{gh})/3 \\ S_1(\mathbf{u}, \mathbf{u}_0): & h \geq h_0, \quad hu = h_0 u_0 + (h - h_0) \sigma_1(\mathbf{u}, \mathbf{u}_0) \end{cases}.$$

is defined as the locus of the right states \mathbf{u} that are connected to the left state \mathbf{u}_0 by means of a direct rarefaction R_1 (Appendix B) or a direct shock S_1 (Appendix C) contained in the first characteristic field. It is possible to demonstrate (Appendix D) that the curve H_1 is continuous, strictly decreasing, and strictly concave. In a similar manner, the backward 2-wave curve

$$(10) \quad H_2^B(\mathbf{u}, \mathbf{u}_0) = \begin{cases} R_2^B(\mathbf{u}, \mathbf{u}_0): & 0 < h \leq h_0, \quad hu = h_0 u_0 - 2(h_0 \sqrt{gh_0} - h \sqrt{gh})/3 \\ S_2^B(\mathbf{u}, \mathbf{u}_0): & h > h_0, \quad hu = h_0 u_0 + (h - h_0) \sigma_2(\mathbf{u}, \mathbf{u}_0) \end{cases}.$$

is defined as the locus of the left states \mathbf{u} that are connected to the right state \mathbf{u}_0 by means of a backward rarefaction R_2^B (Appendix B) or a backward shock S_2^B (Appendix C) contained in the second characteristic field. The curve R_2^B is continuous, strictly increasing, and strictly convex (Appendix D).

In Eqs. (9) and (10), the functions

$$(11) \quad \sigma_1(\mathbf{u}, \mathbf{u}_0) = -\sqrt{0.5g(h+h_0)}, \quad \sigma_2(\mathbf{u}, \mathbf{u}_0) = \sqrt{0.5g(h+h_0)}$$

are the speeds of the shocks contained into the first and the second characteristic field (Appendix C), respectively. It is immediate to show the following

Proposition 2. *The speed of the shocks contained into the first [second] characteristic field of the LInA is always negative [positive].*

Proof. The proposition follows from the signs in Eq. (11).

This is very different from what happens in the SWE, where the sign of the shock speeds depends on the flow characteristics on the two sides of the discontinuity.

3.1.2 Dry bed state and cavitation

In the SWE, the Riemann problem admits solutions where the dry bed is formed also if the bed is initially wet everywhere (Toro 2001). It is interesting to verify if this type of solution, called cavitation, is admissible for the Riemann problem in the LInA equations.

From Eqs. (9) and (10) it is possible to observe that the generic state \mathbf{u}_0 can be connected to the dry bed state $\mathbf{0} = (0 \ 0)^T$ by means of a shock, but not by a rarefaction. In particular, the inspection of Eq. (9) shows that the curve of the right states \mathbf{u} connected to the left dry bed state $\mathbf{0}$ coincides with the direct shock curve

$$(12) \ S_1(\mathbf{u}, \mathbf{0}): \ h \geq 0, \ hu = h\sigma_1(\mathbf{u}, \mathbf{0}).$$

Similarly, the inspection of the Eq. (10) shows that the curve of the left states \mathbf{u} connected to the right dry bed state $\mathbf{0} = (0 \ 0)^T$ coincides with the backward shock curve

$$(13) \ S_2^B(\mathbf{u}, \mathbf{0}): \ h \geq 0, \ hu = h\sigma_2(\mathbf{u}, \mathbf{0}).$$

Notably, the flow velocity corresponding to the state \mathbf{u} behind a shock that advances on the dry bed coincides with the shock celerity, i.e. $u = (hu)/h = \sigma_i(\mathbf{u}, \mathbf{0})$ with $i = 1, 2$. In addition, the Froude number $F(\mathbf{u}) = u/\sqrt{gh}$ corresponding to the state \mathbf{u} connected to the dry bed is constant along the curves $S_1(\mathbf{u}, \mathbf{0})$ and $S_2^B(\mathbf{u}, \mathbf{0})$, and its absolute value is $F_w = \sqrt{0.5} \approx 0.707$.

The presence of a shock connected to the dry bed is opposite to what happens in the SWE, where a generic state is always connected to the dry bed by means of a rarefaction. It is possible to demonstrate the following

Proposition 3. *On the horizontal bed, the Riemann problem of the LInA model admits only solutions with increase of the wetted bed area, while the drying is forbidden.*

Proof. The proposition is proven by contradiction. Under the assumption that a cavitation is forming, a dry bed state $\mathbf{0}$ is found between the left wet state \mathbf{u}_A and the right wet state \mathbf{u}_B , with $\mathbf{u}_A \in S_2^B(\mathbf{u}, \mathbf{0})$ and $\mathbf{u}_B \in S_1(\mathbf{u}, \mathbf{0})$. The speed of the shock between \mathbf{u}_A and $\mathbf{0}$ is positive, and the speed of the shock between \mathbf{u}_B and $\mathbf{0}$ is negative (see *Proposition 2*), meaning that the dry bed between the left state \mathbf{u}_A and the right state \mathbf{u}_B is disappearing. This contradicts the assumption that the bed is drying.

Remark 1. From the proof of *Proposition 3* it is clear that only shocks advancing on the dry bed are possible, while receding shocks are forbidden.

An immediate consequence is the following conclusion:

Proposition 4. *The drying of the wet bed is forbidden.*

Proof. The proposition is a consequence of *Remark 1* and *Proposition 1*. It follows that the LInA model cannot support an authentic bed-drying phenomenon by means of a moving wet-dry frontier.

3.1.3 General solution of the Riemann problem

Given the initial states \mathbf{u}_L and \mathbf{u}_R , the solution of the Riemann problem is complete if the intermediate state \mathbf{u}_M is known. Recalling that \mathbf{u}_M is connected to \mathbf{u}_L by a wave (shock or rarefaction) contained into the first characteristic field, and to \mathbf{u}_R by a wave (shock or rarefaction) contained into the second characteristic field, the intermediate state can be easily found at the intersection of the curves $H_1(\mathbf{u}, \mathbf{u}_L)$ and $H_2^B(\mathbf{u}, \mathbf{u}_R)$. This is equivalent to solving a nonlinear system of two scalar equations, where the unknowns are the components of \mathbf{u}_M . It is possible to demonstrate the following

Proposition 5. *The solution of the Riemann problem for the LInA model on horizontal bed exists if and only if the condition*

$$(14) \quad C: h_L u_L + 2h_L \sqrt{gh_L} / 3 > h_R u_R - 2h_R \sqrt{gh_R} / 3$$

is satisfied. If the solution exists, it is unique.

Proof. The curve $H_1(\mathbf{u}, \mathbf{u}_L)$ is strictly decreasing, and its supremum is

$$(15) \quad \lim_{h \rightarrow 0^+} h u = \lim_{h \rightarrow 0^+} h_L u_L + 2(h_L \sqrt{gh_L} - h \sqrt{gh}) / 3 = h_L u_L + 2h_L \sqrt{gh_L} / 3.$$

Similarly, the curve $H_2^B(\mathbf{u}, \mathbf{u}_R)$ is strictly increasing, and its infimum is

$$(16) \lim_{h \rightarrow 0^+} hu = \lim_{h \rightarrow 0^+} h_R u_R - 2(h_R \sqrt{gh_R} - h \sqrt{gh})/3 = h_R u_R - 2h_R \sqrt{gh_R}/3.$$

This implies that an intersection of the curves $H_1(\mathbf{u}, \mathbf{u}_L)$ and $H_2^B(\mathbf{u}, \mathbf{u}_R)$ exists if and only if the condition of Eq. (14) is satisfied. From the Intermediate value Theorem, it follows that this intersection is unique.

An important consequence of *Proposition 5* is that there is a class of initial conditions, namely those that do not satisfy the Eq. (14), for which the Riemann problem of the LInA Equations has no solution. This is a remarkable difference with respect to the SWE, where the Riemann problem admits a solution for any system of initial conditions (Toro 2001). An example with no solution for the LInA Riemann problem is represented in Figure 1a, with initial data in the first line of Table 1. The inspection of the panel shows that the curves $H_1(\mathbf{u}, \mathbf{u}_L)$ and $H_2^B(\mathbf{u}, \mathbf{u}_R)$ have no intersection, and this implies the absence of solution for the Riemann problem.

It is immediate to see that, depending on the relative position of \mathbf{u}_L and \mathbf{u}_R in the (h, hu) plane, the solution of the Riemann problem for the LInA equations may involve two rarefactions, two shocks, or a shock and a rarefaction. This is in contrast with the existing literature (de Almeida et al. 2012, de Almeida and Bates 2013), where only the shock-rarefaction configuration is admitted. In Figure 1, the curves $H_1(\mathbf{u}, \mathbf{u}_L)$ and $H_2^B(\mathbf{u}, \mathbf{u}_R)$ are plotted for the initial conditions of Table 1, showing that different solution configurations are possible. In particular, an example with two rarefactions is represented in Figure 1b, while a shock-rarefaction and a two shock configuration are represented in Figure 1c and 1d, respectively. In all these cases, the numerical values of h_M and u_M can be found using the Newton-Raphson algorithm, whose convergence is ensured by the regularity of the curves $H_1(\mathbf{u}, \mathbf{u}_L)$ and $H_2^B(\mathbf{u}, \mathbf{u}_R)$.

It is important to note that the dam-break solutions presented in Martins et al. (2016a,b) are just a sub-class (with $u_L = u_R = 0$ m/s) of the general Riemann problem solution presented here.

3.2 Riemann problem on a horizontal dry bed

A comparison between the LInA equations and the SWE can be made by considering the solution of the Riemann problem on a dry bed, with $\mathbf{u}_R = \mathbf{0}$. Recalling the *Proposition 3*, it is evident that the LInA Riemann problem on the dry bed has no solution for $F(\mathbf{u}_L) \leq -2/3$, while the corresponding solution exists in the case of the SWE. For $F(\mathbf{u}_L) > -2/3$, the solution exists and the curve $H_2^B(\mathbf{u}, \mathbf{u}_R)$ reduces to the curve $S_2^B(\mathbf{u}, \mathbf{0})$ of Eq. (13).

It is possible to consider two classes of states \mathbf{u}_L moving on the dry bed, namely the states with $F(\mathbf{u}_L) \in]-2/3, F_w]$ and the states with $F(\mathbf{u}_L) > F_w$. The states \mathbf{u}_L characterized by $F(\mathbf{u}_L) \in]-2/3, F_w]$ are represented in the (h, hu) plane by a point that lies below the curve $S_2^B(\mathbf{u}, \mathbf{0})$. In this case, the intermediate state \mathbf{u}_M between \mathbf{u}_L and $\mathbf{u}_R = \mathbf{0}$ is connected to \mathbf{u}_L by means of a rarefaction contained into the first characteristic field. An example solution (flow depth h) is represented with a continuous line in Figure 2a at time $t = 5$ s for the case $\mathbf{u}_L = (1.00 \quad 0.20)^T$. From the inspection of the figure, it is evident that the flow accelerates along the rarefaction curve from the state \mathbf{u}_L to the state \mathbf{u}_M , which is characterized by $F(\mathbf{u}_M) = F_w$, while the state \mathbf{u}_M is connected to the dry bed by a shock moving with speed $\sigma_2(\mathbf{u}_M, \mathbf{0}) = \sqrt{0.5gh_M}$. The slowest signal of this solution configuration is the left edge of the rarefaction wave, which moves with speed $\lambda_l(\mathbf{u}_L) = -\sqrt{gh_L}$. The solution of the SWE for the same problem is characterized by a rarefaction connecting the state \mathbf{u}_L to the dry bed, and it is represented in Figure 2a with a dashed line. In the SWE solution, the slowest edge of the rarefaction wave moves with speed $\lambda_{SLOW} = u_L - \sqrt{gh_L}$, while the fastest edge of the rarefaction wave moves with speed $\lambda_{FAST} = u_L + 2\sqrt{gh_L}$.

When the state \mathbf{u}_L is characterized by $F(\mathbf{u}_L) > F_w$, it lies above the curve $S_2^B(\mathbf{u}, \mathbf{0})$ of the (h, hu) plane. In this case, the intermediate state \mathbf{u}_M between \mathbf{u}_L and $\mathbf{u}_R = \mathbf{0}$ is connected to \mathbf{u}_L by a

shock contained into the first characteristic field. An example solution (flow depth h) is represented in Figure 2b at time $t = 5$ s for the case $\mathbf{u}_L = (1.00 \quad 5.00)^T$. The inspection of the panel shows that the shock connecting the states \mathbf{u}_L and \mathbf{u}_M moves upstream with speed $\sigma_1(\mathbf{u}_M, \mathbf{u}_L) = -\sqrt{0.5g(h_M + h_L)}$, slowing down the state \mathbf{u}_L to subcritical flow conditions characterized by $F(\mathbf{u}_M) = F_w$, while the downstream shock moves with speed $\sigma_2(\mathbf{u}_M, \mathbf{0}) = \sqrt{0.5gh_M}$. The appearance of the upstream shock is an unphysical feature of the solution that is not exhibited by the SWE, whose exact solution is plotted with a dashed line in the same panel.

It is useful to compare the slowest and the fastest wave speeds exhibited by LInA and SWE for the Riemann problem on dry bed. The coefficient ρ_{SLOW} is the ratio between the slowest waves in the SWE and in the LInA equations solutions, and it is defined as

$$(17) \quad \rho_{SLOW} = \begin{cases} F(\mathbf{u}_L) \in [-2/3, F_w], & (u_L - \sqrt{gh_L}) / \lambda_1(\mathbf{u}_L) \\ F(\mathbf{u}_L) > F_w, & (u_L - \sqrt{gh_L}) / \sigma_1(\mathbf{u}_M, \mathbf{u}_L) \end{cases},$$

while ρ_{FAST} is the ratio between the fastest waves in the SWE and in the LInA equations solutions, and it is defined as

$$(18) \quad \rho_{FAST} = (u_L + 2\sqrt{gh_L}) / \sigma_2(\mathbf{u}_M, \mathbf{0}).$$

The coefficients ρ_{SLOW} and ρ_{FAST} are plotted in Figure 3 for $F(\mathbf{u}_L) \in [-0.5, 2]$. The slowest wave in the LInA solution is similar to that of the SWE solution when $F(\mathbf{u}_L)$ is close to zero. In particular, the percentage error is less than 20% for $F(\mathbf{u}_L) \in [-0.2, 0.2]$, but it increases rapidly for

$|F(\mathbf{u}_L)| > 0.2$. Very interestingly, both the slowest waves keep the negative sign for $F(\mathbf{u}_L) < 1$, while the sign of the slowest wave in the SWE solution becomes positive for supercritical flows. Finally, the figure shows that in the interval considered the fastest wave of the SWE solution is at least 3.83 times greater than the fastest wave of the LInA solution. In other words, the LInA equations strongly underestimate the speed of the wetting phenomenon on a frictionless horizontal dry bed.

3.3 Impact on a wall

The impact on a wall can be simulated by considering a Riemann problem where $h_R = h_L$, and $u_R = -u_L$ (Toro 2001). In Figure 4a, the exact solution (flow depth) of the LInA equations is represented with a continuous line at time $t = 5$ s for the case $\mathbf{u}_L = (1.00 \quad 1.50)^T$. The inspection of the panel shows that the impact on the wall causes the increase of the flow depth, and the formation of a shock moving upstream that decelerates the flow to the rest. In the same panel, the solution for the SWEs is represented with a dashed line. The comparison between the plots shows that the SWEs produce a higher flow depth at the wall, while the speed of the backward shock is smaller.

The ratio h_{LIna}/h_{SWE} between the wall flow depths supplied by the two mathematical models is represented in Figure 4b for different values of the incoming flow Froude number $F(\mathbf{u}_L)$. From the figure, it is evident that the error is greater than 5% for $F(\mathbf{u}_L) > 0.45$, and it is greater than 10% for $F(\mathbf{u}_L) > 0.70$.

4 Exact solution for floodplain wetting with friction

The formation of shocks is not limited to the case of Riemann problem on a dry bed without friction. In order to show that this is what always happens in general cases, it is sufficient to consider the propagation of a nonbreaking wave on a horizontal bed with uniform velocity.

Following an analysis similar to that made by Hunter et al. (2005) for the SWE, the system of Eq. (2) is solved with initial flow depth $h_0(x) = h(x, 0)$ and constant uniform flow velocity $u(x, t) = u_0 > 0$. If the Chézy formula is used for the calculation of the friction slope S_f , the LInA model can be simplified as follows:

$$(19) \quad \begin{aligned} \frac{\partial h}{\partial t} + u_0 \frac{\partial h}{\partial x} &= 0 \\ u_0 \frac{\partial h}{\partial t} + gh \frac{\partial h}{\partial x} &= -g \frac{u_0^2}{C^2}, \end{aligned}$$

where C is the Chézy coefficient. It is evident that the first of Eq. (19) coincides with the linear advection equation (LeVeque 1992), which admits exact solution

$$(20) \quad h(x, t) = h_0(x - u_0 t).$$

The Eq. (20) implies that the flow profile translates rigidly with velocity u_0 . If $h'_0(x)$ is the derivative of the initial flow depth $h_0(x)$, the second of Eq. (19) can be rewritten as an ordinary differential equation, as follows:

$$(21) \quad (gh_0 - u_0^2)h'_0 = -g \frac{u_0^2}{C^2}.$$

From Eq. (21), it is confirmed that the flow profile cannot be continuously connected to the dry bed. In fact, the flow profile slope h'_0 corresponding to $h_0 = 0$ is positive, and this configuration must be excluded because it is equivalent to a condition where the free surface profile is emerging from the dry bed. The only remaining possibility is that the smooth part of the flow profile is connected to the dry bed by a shock that is contained into the second characteristic field and whose celerity is $\sigma_2 = u_0$. From Eq. (11), it follows that the flow behind this shock is characterized by flow depth $h_F = (2u_0^2)/g$ and Froude number $F_F = u_0/\sqrt{gh_F} = F_w$. If the initial abscissa corresponding to the shock is x_F , the initial flow profile slope corresponding to the depth $h_F = h_0(x_F)$ is $\lim_{x \rightarrow x_F} h'_0(x) = -g/C^2$, and this implies that the initial flow depth h_0 increases from downstream to upstream.

The Eq. (21) can be solved by separation of variables, obtaining

$$(22) \quad h_0(x) = \begin{cases} x < x_F, & h_B \left[F_B^2 + \sqrt{\left(1 - F_B^2\right)^2 - \frac{x}{x_0}} \right], \\ x > x_F, & 0 \end{cases}$$

where $x_0 = C^2 h_B / (2gF_B^2)$, $h_B = h_0(0)$ is the flow depth at the reference abscissa $x = 0$ and $F_B = u_0/\sqrt{gh_B}$ is the corresponding Froude number, while the shock position x_F is defined by

$$(23) \quad x_F = x_0 - \frac{C^2 h_B}{g}.$$

The bound $h_B \geq h_F$ implies that only the subcritical reference conditions characterized by $F_B \leq F_w$ can be imposed to the LInA model for this problem. The application of a similar procedure to the SWE of Eq. (1) leads to the solution

$$(24) \quad h_0(x) = \begin{cases} x \leq x_0, & h_B \sqrt{1 - \frac{x}{x_0}} \\ x > x_0, & 0 \end{cases}$$

No additional bound is imposed to $h_B > 0$ in Eq. (24), and this means that the flow profile corresponding to the SWE can be constructed not only for $F_B \leq F_w$, but also for the case $F_B > F_w$.

The flow profile of Eq. (22) can be represented in the plane $(\xi, h_0/h_B)$, where the dimensionless distance is defined by $\xi = x/x_0$. The cases $F_B = 0.3$ (thick dashed line) and $F_B = 0.5$ (thick solid line) are plotted in the Figure 5, where the flow profile of Eq. (24) corresponding to the SWE is also represented with a thin solid line. The inspection of Figure 5 shows that the solution corresponding to the LInA model approximates the SWE solution for $F_B = 0.3$, while a well developed shock at the front of the advancing wave is present for values $F_B = 0.5$, which is closer to the limit F_w . As expected from *Proposition 1*, the shock at the front of the LInA equations solution disappears in the limit $F_B \rightarrow 0$, where Eqs. (22) and (24) coincide.

As a final comment, it must be observed that the Figures 9 and 10 contained in the work by de Almeida and Bates (2013) correspond to the numerical solution with LInA of the nonbreaking wave propagation on a horizontal plane and on adverse slope, respectively. In both figures, the leading shock at the wave edge is evident. Surprisingly, this feature of LInA has never been recognized and discussed before.

5 Solution of the Riemann problem on uneven bed

Geometric singularities such as terrain steps and drops, sills, embankment and levee sides, channel sidewalls, sidewalk steps, walls, and buildings, are commonly present in the flooded areas. These features, which are all characterized by a rapid variation of the terrain elevation, can be modeled by bed elevation discontinuities (Cozzolino et al. 2011). Recalling that the leading edge of flooding waves in the LInA model is always represented by a discontinuity moving on dry bed, it is interesting to consider the interaction between such a discontinuity and the bed elevation discontinuities. This task can be properly tackled in the context of an augmented Riemann problem, where the bed elevation is added among the conserved variables.

The systematic analysis of the Riemann problem on uneven bed in the LInA model is beyond the scope of the present paper, and for this reason only some example will be considered. The corresponding results will be compared with those supplied by the SWE, for which the solution of the discontinuous-bed Riemann problem is discussed in Alcrudo and Benkhaldoun (2001).

5.1 Position of the Riemann problem and general solution

When the bed is not horizontal, it is possible to consider an augmented system of partial differential equations obtained by adding the trivial equation $\partial z / \partial t = 0$ to the system of Eq. (6). In vector form, the augmented system is rewritten as

$$(25) \quad \frac{\partial \mathbf{U}}{\partial t} + \frac{\partial \mathbf{F}(\mathbf{U})}{\partial x} + \mathbf{H}(\mathbf{U}) \frac{\partial \mathbf{U}}{\partial x} = 0,$$

where $\mathbf{U}(x, t) = (h \quad hu \quad z)^T$ is the augmented vector of the conserved variables, $\mathbf{F}(\mathbf{U}) = (hu \quad gh^2/2 \quad 0)^T$ is the augmented vector of the fluxes, while the matrix $\mathbf{H}(\mathbf{U})$ is defined as

$$(26) \quad \mathbf{H}(\mathbf{U}) = \begin{pmatrix} 0 & 0 & 0 \\ 0 & 0 & gh \\ 0 & 0 & 0 \end{pmatrix}.$$

It is easy to see that the matrix $\mathbf{A}(\mathbf{U}) = \partial \mathbf{F} / \partial \mathbf{U} + \mathbf{H}(\mathbf{U})$ has the following three distinct real eigenvalues

$$(27) \quad \lambda_1(\mathbf{U}) = -\sqrt{gh}, \quad \lambda_0(\mathbf{U}) = 0, \quad \lambda_2(\mathbf{U}) = \sqrt{gh},$$

with corresponding linearly independent eigenvectors

$$(28) \quad \mathbf{r}_1(\mathbf{U}) = \begin{pmatrix} 1 & -\sqrt{gh} & 0 \end{pmatrix}^T, \quad \mathbf{r}_0(\mathbf{U}) = \begin{pmatrix} 1 & 0 & -1 \end{pmatrix}^T, \quad \mathbf{r}_2(\mathbf{U}) = \begin{pmatrix} 1 & \sqrt{gh} & 0 \end{pmatrix}^T.$$

It is evident that the system of Eq. (25) is strictly hyperbolic, and that it differs from the system of Eq. (6) because the conserved variable z has introduced an additional characteristic field. The same arguments used in Appendix A for the system of Eq. (6) can be used to show that the characteristic fields related to the eigenvectors $\mathbf{r}_1(\mathbf{U})$ and $\mathbf{r}_2(\mathbf{U})$ are genuinely non-linear, and that they may contain moving waves such as shocks or rarefactions. Interestingly, the third component of the vectors $\mathbf{r}_1(\mathbf{U})$ and $\mathbf{r}_2(\mathbf{U})$ is null, and this means that the shocks and the rarefactions contained in the corresponding characteristic fields may develop only where the bed elevation is constant. The comparison between Eq. (28) and Eq. (7) leads to the conclusion that the projection on the (h, hu) plane of 1- and 2-waves coincides with the expressions of Eqs. (9) and (10).

Special attention should be paid to the characteristic field corresponding to the eigenvector $\mathbf{r}_0(\mathbf{U})$. It is immediate to see that this characteristic field is linearly degenerate, because

$\nabla^T \lambda_0(\mathbf{U}) \mathbf{r}_0(\mathbf{U}) = 0$, and this means that the 0-waves contained into this characteristic field are special discontinuities called contact discontinuities.

The Riemann problem consists in solving Eq. (25) with initial conditions

$$(29) \quad \mathbf{U}(x, 0) = \begin{cases} x < 0, & \mathbf{U}_L \\ x > 0, & \mathbf{U}_R \end{cases},$$

where $\mathbf{U}_L = (h_L \ h_L u_L \ z_L)^T$ and $\mathbf{U}_R = (h_R \ h_R u_R \ z_R)^T$. Also in this case, the solution of the Riemann problem is self-similar, and a vector function $\mathbf{V}(s)$ of the scalar parameter s exists such that $\mathbf{U}(x, t) = \mathbf{V}(x/t)$. Recalling that $\lambda_1(\mathbf{U}) < \lambda_0(\mathbf{U}) < \lambda_2(\mathbf{U})$, it is immediate to see that the solution of the Riemann problem consists in the four ordered states \mathbf{U}_L , $\mathbf{U}_1 = (h_1 \ h_1 u_1 \ z_L)^T$, $\mathbf{U}_2 = (h_2 \ h_2 u_2 \ z_R)^T$, and \mathbf{U}_R , where \mathbf{U}_L and \mathbf{U}_1 are connected by a 1-wave, \mathbf{U}_1 and \mathbf{U}_2 are connected by a 0-wave, while \mathbf{U}_2 and \mathbf{U}_R are connected by a 2-wave. In the following, the symbols $\mathbf{u}_L = (h_L \ h_L u_L)^T$, $\mathbf{u}_R = (h_R \ h_R u_R)^T$, $\mathbf{u}_1 = (h_1 \ h_1 u_1)^T$, and $\mathbf{u}_2 = (h_2 \ h_2 u_2)^T$, are used to indicate the projections on the (h, hu) plane of the vectors \mathbf{U}_L , \mathbf{U}_R , \mathbf{U}_1 , and \mathbf{U}_2 , respectively.

5.2 Definition of the contact discontinuity

It is easy to see that the speed of the discontinuities contained into the characteristic field associated to $\mathbf{r}_0(\mathbf{U})$ is null. In fact, the application of the Rankine-Hugoniot condition (LeVeque 1992) to the trivial equation $\partial z / \partial t = 0$ leads to

$$(30) \quad (z_R - z_L) \sigma_0(\mathbf{U}_1, \mathbf{U}_2) = 0,$$

because the corresponding flux is identically null. The Eq. (30) implies that the speed $\sigma_0(\mathbf{U}_1, \mathbf{U}_2)$ of the discontinuities contained in the 0-th characteristic field is null for $z_R - z_L \neq 0$, and that the constant states \mathbf{U}_1 and \mathbf{U}_2 connected by the 0-wave are located to the left and to the right of $x = 0$, respectively.

The mathematical relationship between \mathbf{U}_1 and \mathbf{U}_2 can be constructed by observing that the characteristic field corresponding to the eigenvector $\mathbf{r}_0(\mathbf{U})$ can be associated to the steady flow solutions of Eq. (25). In fact, these solutions satisfy the condition

$$(31) \quad \mathbf{A}(\mathbf{U}) \frac{\partial \mathbf{U}}{\partial x} = 0,$$

which means that $\partial \mathbf{U} / \partial x$ must be proportional to an eigenvector of \mathbf{A} with identically null eigenvalue. This eigenvector is precisely $\mathbf{r}_0(\mathbf{U})$, and the proportionality equation

$$(32) \quad \frac{\partial \mathbf{U}}{\partial x} = \alpha(x) \mathbf{r}_0(\mathbf{U}(x)),$$

is a differential equation with solution $z + h = \text{const.}$ and $hu = \text{const.}$ (see Appendix E). It is easy to verify that this solution remains meaningful in the case of bed elevation discontinuity, and this suggests to define the 0-wave as

$$(33) \quad H_0(\mathbf{U}_2, \mathbf{U}_1) = \begin{cases} h_1 u_1 = h_2 u_2 \\ z_L + h_1 = z_R + h_2 \end{cases}.$$

The 0-wave definition of Eq. (33) coincides with the choice made by Aronica et al. (1998) for the inner boundary conditions characterized by rapid variations of the bed elevation.

5.3 Riemann problem at the dry bed step

The Riemann problem at the dry bed step consists in solving the system of Eq. (25) with initial conditions of Eq. (29), where $h_R = 0$ m, $h_{RUR} = 0$ m²/s, and $z_L < z_R$. The problem can be solved by finding the projections \mathbf{u}_1 and \mathbf{u}_2 of \mathbf{U}_1 and \mathbf{U}_2 on the plane (h, hu) , respectively, that satisfy the Eq. (33) and that lie on the curves $H_1(\mathbf{u}, \mathbf{u}_L)$ and $H_2^B(\mathbf{u}, \mathbf{0})$, respectively. Instead of doing a systematic analysis of all the possible solution configurations, as made in Section 2 for the Riemann problem on horizontal bed, some example solution will be considered in the present subsection, in order to discuss the differences between the LInA model and the SWE on uneven bed. The initial data for the examples considered are resumed in Table 2, while the corresponding solutions at time $t = 5$ s (free surface elevation) are plotted in Figure 6.

The panel of Figure 6a (continuous line) corresponds to the case where the incoming flow is subcritical ($F(\mathbf{u}_L) = 0.064 < F_w$), and the corresponding energy is higher than that strictly required to pass over the obstacle. The state \mathbf{U}_L is connected to the state \mathbf{U}_1 by a rarefaction, while the state \mathbf{U}_2 over the bed step is connected to the dry bed on the step by a shock. The Froude number corresponding to the flow moving on the dry bed is fixed, and equal to $F(\mathbf{u}_2) = F_w$, as shown in Subsection 3.1.2. The solution of the SWE for the same problem is represented with a dashed line, and exhibits a right rarefaction whose celerity is greater than the celerity of the fastest signal in the LInA equations. Notably, the underestimation of the fastest signal does not correspond to an underestimation of the discharge over the bed step, because the discharge per unit width through the geometric discontinuity exhibited by the LInA equations is $h_1 u_1 = 0.537$ m²/s, and it is higher than the value $h_1 u_1 = 0.459$ m²/s corresponding to the Shallow water Equations, while the flood stage immediately to the left of the obstacle is similar. If $H(\mathbf{U}) = h + u^2/(2g) + z$ is the total head related to the generic state \mathbf{U} , it is immediate to see that $H(\mathbf{U}_1) - H(\mathbf{U}_2) = -0.079$ m, meaning that the

energy of the flow is increased through the geometric discontinuity. In absence of external devices such as pumps, this phenomenon is clearly unphysical.

The Figure 6b represents a subcritical case (initial data in Table 2, with $F(\mathbf{u}_L) = 0.479 < F_w$) where the bed step in the LInA Riemann problem is high enough to completely reflect the incoming flow from the left, leaving the top of the bed step dry. The SWE exhibit a totally different behavior (dashed line in Figure 6b) for the same data, because the energy is sufficient to make the flow jump over the bed step.

In Figure 6c it is represented the case where the incoming flow is supercritical (initial data in Table 2, with $F(\mathbf{u}_L) = 1.596 > F_w$) and the dry bed step is high enough to partially reflect the flow ($z_R - z_L = 0.50$ m). For this reason, the solution of the LInA equations exhibit a fast shock that moves backward, while a slower shock propagates over the dry bed step. The flow depth immediately to the left of the geometric discontinuity is $h_1 = 1.640$ m, while the discharge passing through the geometric discontinuity is $h_1 u_1 = 2.696$ m²/s. On the contrary, the Shallow water Equations (dashed line) exhibit a shock that propagates backward very slowly, but a fast rarefaction propagates on the dry step. In the example of Figure 6c, the LInA model underestimates not only the flooded area, but also the discharge through the geometric discontinuity and the flood stage, because the SWE predict $h_1 u_1 = 4.203$ m²/s and $h_1 = 2.126$ m. In addition, the LInA model predicts an increase of energy through the geometric discontinuity, because $H(\mathbf{U}_1) - H(\mathbf{U}_2) = -0.147$ m.

The example solution of Figure 6d can be instructively compared with that of Figure 6c, because the characteristics of the incoming flow are identical, while the bed step is significantly lower ($z_R - z_L = 0.10$ m). In this case, the LInA equations predict again the partial reflection of the flow against of the obstacle (continuous line), with flow depth $h_1 = 1.446$ m and discharge $h_1 u_1 = 3.457$ m²/s. The structure of the solution corresponding to the Shallow water Equations (dashed line) is very different, because it corresponds to the complete transmission of the incoming wave, which has sufficient energy to jump over the bed step without reflection. In particular, $h_1 = h_L$,

while the discharge over the bed step predicted by the Shallow water Equations is $h_1 u_1 = 5 \text{ m}^2/\text{s}$. This confirms that the Shallow water Equations are able to make the flow jump over obstacles that reflect partially or totally the waves computed by the LInA equations. Also in this case, the LInA equations predict an increase of energy through the geometric discontinuity, because $H(\mathbf{U}_1) - H(\mathbf{U}_2) = -0.045 \text{ m}$.

5.4 Riemann problem at the dry bed drop

When the Riemann problem at the bed drop is considered, the system of Eq. (25) is solved with the initial conditions of Eq. (29), where $h_R = 0 \text{ m}$, $h_R u_R = 0 \text{ m}^2/\text{s}$, and $z_L > z_R$. The initial data for the examples considered in the present subsection are reported in Table 3, while the corresponding solution at time $t = 5 \text{ s}$ (free surface elevation) is plotted in Figure 7.

In Figure 7a, the solution of the Riemann problem is represented for the same flow conditions of Figure 6a, (subcritical incoming flow with $F(\mathbf{u}_L) = 0.064 < F_w$), but now there is a bed drop ($z_R - z_L = -0.20 \text{ m}$) instead of a bed step. The incoming flow \mathbf{U}_L is connected to the state \mathbf{U}_1 to the left of the geometric discontinuity by a rarefaction, while the state \mathbf{U}_2 to the right of the geometric discontinuity is connected to the dry bed on the step by a shock. The flow \mathbf{U}_1 at the top of the bed drop is expected to be critical, but the LInA equations supply a supercritical flow, characterized by Froude number $F(\mathbf{u}_1) = 1.126$ and velocity $u_1 = 2.615 \text{ m/s}$, while the Froude number corresponding to the flow moving on the dry bed is fixed, and equal to $F(\mathbf{u}_2) = F_w$. The solution of the SWEs for the same problem is represented with a dashed line, and consists of a rarefaction that accelerates the incoming flow until the critical conditions are attained immediately to the left of the bed drop ($F(\mathbf{u}_1) = 1$), while the supercritical flow ($F(\mathbf{u}_2) = 2.052$) at the foot of the bed drop is connected to the dry bed by a rarefaction. The LInA equations underestimate the fastest signal, but overestimate the discharge passing through the geometric discontinuity ($h_1 u_1 =$

$1.437 \text{ m}^2/\text{s}$ instead of $h_1 u_1 = 1.012 \text{ m}^2/\text{s}$). Interestingly, $H(\mathbf{U}_1) - H(\mathbf{U}_2) = -0.161 \text{ m}$, meaning that the energy of the flow is loss through the geometric discontinuity.

In the case of Figure 7b, the characteristics of the incoming flow coincide with those of Figure 7a, but now the bed drop is higher ($z_R - z_L = -1.01 \text{ m}$). Despite the similarity of the solution structure with that of Figure 7a, the velocity associated to the state \mathbf{U}_1 is now $u_1 = 203.760 \text{ m/s}$, with flow depth $h_1 = 0.011 \text{ m}$, and this means that the velocity of supercritical flows at the top of the bed drop depends on the height of the drop, which is clearly unphysical. This aspect will be examined in the next subsection. Due to the high value of the flow velocity u_1 , the head $H(\mathbf{U}_1) = 2116.134 \text{ m}$ is out of the range of values encountered in practical applications, and the head loss $H(\mathbf{U}_1) - H(\mathbf{U}_2) = 2115.867 \text{ m}$ at the geometric discontinuity is correspondingly high.

In Figure 7c, the subcritical incoming flow ($F(\mathbf{u}_L) = 0.836 > F_w$) encounters a small bed drop. The classic SWE supply a solution (dashed line) where the flow is accelerated towards the critical state at the top of the bed drop by means of a rarefaction, while the flow is supercritical at the step foot. On the contrary, the LInA model supplies a solution configuration where the flow is decelerated by a shock connecting the states \mathbf{U}_L and \mathbf{U}_1 that moves backward, while the flow \mathbf{U}_2 at the step foot is subcritical. The head loss $H(\mathbf{U}_1) - H(\mathbf{U}_2) = 0.005 \text{ m}$ at the geometric discontinuity is very low, in this case.

A case where the incoming flow is supercritical ($F(\mathbf{u}_L) = 1.596 > F_w$) is represented in Figure 7d. The SWE supply a solution where this flow is not influenced by the presence of the bed drop, while the solution corresponding to the LInA model exhibits a rarefaction that propagates upstream. The head loss through the geometric discontinuity is $H(\mathbf{U}_1) - H(\mathbf{U}_2) = 1.759 \text{ m}$, and it is quite high.

5.5 Limits of existence for the Riemann problem at the dry bed drop

The case of Figure 7b seems very close to the applicability limits of the LInA model because the water depth at the top of the bed drop is close to zero, while the velocity is very high and out of the range of practical applications. These observations stimulate a closer analysis of the Riemann problem at the dry bed drop, in order to plot a diagram with the fields of existence of the different types of solution.

Preliminarily, it is observed that the Froude number of the flow at the top of the bed drop is constrained by the drop height. In fact, it is immediate to see that the projection \mathbf{u}_2 of \mathbf{U}_2 on the (h, hu) plane must lie on the curve $S_2^B(\mathbf{u}, \mathbf{0})$, while the states \mathbf{U}_1 and \mathbf{U}_2 must satisfy the Eq. (33). The two conditions lead to the solution

$$(34) \quad F(\mathbf{u}_1) = F_w \left(1 + \frac{a}{h_1} \right)^{3/2},$$

where $a = z_L - z_R > 0$ is the step height. It is immediate to see that a shock connects the state \mathbf{U}_L to the state \mathbf{U}_1 when $F(\mathbf{u}_L) > F(\mathbf{u}_1)$, while a rarefaction connects the state \mathbf{U}_L to the state \mathbf{U}_1 when $F(\mathbf{u}_L) < F(\mathbf{u}_1)$. The position $\mathbf{U}_L = \mathbf{U}_1$ leads to the limiting condition

$$(35) \quad F(\mathbf{u}_L) = F_w \left(1 + \frac{a}{h_L} \right)^{3/2}$$

between the solutions with a shock and the solutions with a rarefaction. The Eq. (35) is represented in the plane $(F(\mathbf{u}_L), a/h_L)$ of Figure 8 with a dashed line.

If the left Froude number $F(\mathbf{u}_L)$ is less than the limit of Eq. (35) for a given value of a/h_L , a rarefaction contained in the first characteristic field connects the states \mathbf{U}_L and \mathbf{U}_1 , and this implies

that \mathbf{u}_1 lies on the curve $R_i(\mathbf{u}, \mathbf{u}_L)$. After the position $\mathbf{u} = \mathbf{u}_1$ and $\mathbf{u}_0 = \mathbf{u}_L$ in Eq. (9), and the substitution in Eq. (34), some algebra leads to

$$(36) \quad F_w \left(\frac{h_1}{h_L} + \frac{a}{h_L} \right)^{3/2} = F(\mathbf{u}_L) + \frac{2}{3} \left[1 - \left(\frac{h_1}{h_L} \right)^{3/2} \right]$$

which makes sense only for $h_1 > 0$. The limit $h_1 \rightarrow 0$ leads to the condition

$$(37) \quad F(\mathbf{u}_L) = F_w \left(\frac{a}{h_L} \right)^{3/2} - \frac{2}{3},$$

which is represented in Figure 8 with a continuous line. The initial conditions which are close to the limit of Eq. (37) lead to arbitrarily high values of the velocity u_1 , and this explains the results of the Riemann problem depicted in Figure 7b. The region above the curve of Eq. (37) is forbidden, and this implies that there are initial conditions for the Riemann problem at the dry bed drop that do not admit any solution. This is in contrast with the SWE, where the solution of the Riemann problem at bed elevation discontinuities always exists.

6 Numerical experiments

In this section, the characteristics of a widely used numerical model for the approximate solution of the LInA, namely the *q-centered* finite-difference scheme by de Almeida et al. (2012), are verified with reference to the flood propagation computation. The original algorithm is then modified in order to ensure depth-positivity.

6.1 The *q-centered* scheme by de Almeida et al. (2012)

In the *q-centered* scheme, which is an improvement of the staggered-grid finite-difference scheme by Bates et al. (2010), the flow field is subdivided into rectangular cells of length Δx . The variables z_i , h_i , and $\zeta_i = h_i + z_i$ (free surface elevation), are stored at the center of the i -th cell, while the discharge $q_{i-1/2}$ is stored at the interface between the cells $i-1$ and i . In the one-dimensional case, the discharge $q_{i-1/2}$ is advanced from the time level t^n to the time level t^{n+1} by means of the following non-conservative scheme:

$$(38) \quad q_{i-1/2}^{n+1} = \theta q_{i-1/2}^n + \frac{1-\theta}{2} (q_{i-3/2}^n + q_{i+1/2}^n) - \lambda g h_{f,i-1/2}^n (\zeta_i^n - \zeta_{i-1}^n),$$

where $h_{f,i-1/2}^n = \max[\zeta_{i-1}^n, \zeta_i^n] - \max[z_{i-1}, z_i]$, $\theta \in [0,1]$ is an user-defined coefficient, $\Delta t = t^{n+1} - t^n$ is the time step, and $\lambda = \Delta t / \Delta x$. Once that the discharge at the interfaces has been adjourned, the free-surface elevation in the cells is advanced in time by means of the conservative scheme

$$(39) \quad h_i^{n+1} = h_i^n - \lambda (q_{i+1/2}^{n+1} - q_{i-1/2}^{n+1}).$$

If $h_i^{n+1} < 0$, the position $h_i^{n+1} = 0$ is made: in this case, the global mass conservation mass is violated but $h_i^{n+1} \geq 0$ everywhere. For linear stability requirements, the time step Δt used at the time level t^n satisfies the inequality $\Delta t \leq \Delta t_0$, where

$$(40) \quad \Delta t_0 = \min \left[\Delta t_{\max}, \alpha \frac{\Delta x}{\sqrt{g h_{\max}^n}} \right].$$

In Eq. (40), $h_{\max}^n = \max_i \{h_i^n\}$ is the maximum flow depth within the computational domain at the time level t^n , $\alpha \in (0, 1]$ is an user defined coefficient, and Δt_{\max} is the maximum allowed time step for accuracy purposes. In the following, the coefficients $\alpha = 0.7$ (de Almeida et al. 2012), $\theta = 0.7$ (de Almeida and Bates 2013), $\Delta t_{\max} = 0.1$ s, and $\Delta t = \Delta t_0$ are constantly used.

6.1.1 Riemann problems on flat bed

The *q-centered* scheme by de Almeida et al. (2012) is applied to two Riemann problems on flat dry bed. The first Riemann problem is characterized by $\mathbf{u}_L = (1.00 \quad 5.00)^T$ and $\mathbf{u}_R = (0 \quad 0)^T$, and the results of the calculations corresponding to the channel with length $L = 100$ m ($\Delta x = 0.02$) are represented for $t = 5.002$ s in Figure 9a with a dashed line (flow depth). The comparison with the exact solution (continuous thick line) shows that the celerity and the strength of the shocks are only approximately captured, and this is expected for numerical schemes that are written in non-conservative form (Hou and LeFloch 1994). In particular, the *q-centered* scheme is not able to capture the strength and the propagation celerity of the wetting front, and the error about the corresponding position increases with time. During the simulation, the theoretical variation of water volume contained in the channel can be calculated with $\Delta W(t) = h_L u_L t$, and this supplies the theoretical volume of water contained into the physical domain at the end of calculations. In the present case, the relative difference between the computed final volume and the theoretical final volume is $5.68 \cdot 10^{-16}$, which is close to the machine error.

The second Riemann problem is characterized by $\mathbf{u}_L = (1.00 \quad -5.00)^T$ and $\mathbf{u}_R = (0 \quad 0)^T$. Despite the fact that the LInA equations do not admit an exact solution for this Riemann problem on the dry bed ($F(\mathbf{u}_L) \leq -2/3$), the numerical model computes a solution whose results are represented with a dashed line in Figure 9b for $t = 5.002$ s. The inspection of the figure shows that the *q-centered* numerical model exhibits a rarefaction, with flow moving towards the left. In the

channel of length $L = 100$ m, the relative difference between the computed final volume and the theoretical final volume is 0.399, which is far out of the admissible range for the practical applications.

6.1.2 Oscillations in the parabolic channel

Thacker (1981) has supplied the exact solution for the oscillations of the SWE in a one-dimensional frictionless rectangular channel with bed elevation described by

$$(41) \quad z(x) = z_0 \left(\frac{x}{a} \right)^2,$$

where a , and z_0 are parameters. At time $t = 0$ s, the initial velocity is null, while the initial flow depth is described by

$$(42) \quad h(x, 0) = \max \left[0, \zeta_0 - \frac{u_{\max} \omega}{g} x - z(x) \right],$$

where u_{\max} and ζ_0 are parameters, while $\omega = \sqrt{2z_0 g} / a$. For $t > 0$ s, the mass oscillates with period $T = 2\pi/\omega$, maintaining a planar free surface profile. The exact solution for the flow depth is described by

$$(43) \quad h(x, t) = \max \left[0, \zeta_0 - \frac{u_{\max} \omega}{g} x \cos \omega t + \frac{u_{\max}^2}{2g} (1 - \cos^2 \omega t) - z(x) \right],$$

and the maximum flow depth through the domain is $h_{\max} = \zeta_0 + u_{\max}^2 / (2g)$.

The *q-centered* scheme by de Almeida et al. (2012) is applied with $\Delta x = 0.12$ m to the case with parameters $a = 2000$ m, $z_0 = 4$ m, $\zeta_0 = 3$ m, $u_{max} = 2$ m/s, and the corresponding results are represented in Figure 10 for the times $t_1 = 350.17$ s (Figure 10a), $t_2 = 710.39$ s (Figure 10b), $t_3 = 1060.57$ s (Figure 10c), and $t_4 = 1420.73$ s (Figure 10d). In the same figure, the exact solution of the SWE is also represented. The inspection of the diagram shows that there is no general agreement between the LInA *q-centered* numerical solution and the SWE exact solution, because the average free surface slope is not well captured, together with the position of the wetting-drying fronts. The maximum value of the flow depth predicted by the numerical model is $h_{max} = 4.34$ m, and it is 35% greater than the exact value. The main reason of this discrepancy seems the lack of mass conservation by the numerical algorithm. For example, the relative difference between the numerical and exact volume at time t_4 is 0.541, and this is clearly unacceptable. Interestingly, the *q-centred* scheme by de Almeida et al. (2012) supplies receding wet-dry fronts that are continuously connected with the dry bed, and this is in contrast with the LInA equations, which do not admit such a solution feature.

Corresponding to the value calculated for h_{max} , the minimum time step used by the algorithm is $\Delta t_{min} = 0.0129$ s.

6.2 A modified *q-centered* scheme

The preceding calculations prompt a modification of the scheme by de Almeida et al. (2012) that is able to preserve depth-positivity at every step of the algorithm. Aiming at this, we observe that the substitution of Eq. (38) into Eq. (39) leads to

$$(44) \quad h_i^{n+1} = h_i^n - \frac{\lambda}{2} \left[(3\theta - 1)(q_{i+1/2}^n - q_{i-1/2}^n) + (1 - \theta)(q_{i+3/2}^n - q_{i-3/2}^n) \right] + \\ - \lambda^2 \left[gh_{f,i+1/2}^n (\zeta_{i+1}^n - \zeta_i^n) - gh_{f,i-1/2}^n (\zeta_i^n - \zeta_{i-1}^n) \right].$$

The inspection of Eq. (44) shows that h_i^{n+1} varies quadratically with λ , and that $h_i^{n+1} \rightarrow h_i^n$ for $\lambda \rightarrow 0$. When $h_i^n > 0$, a continuity argument proves that there exists a sufficiently small time step $\Delta t > 0$ in the neighborhood of $\Delta t = 0$ that is able to ensure the condition $h_i^{n+1} \geq 0$ when $h_i^n > 0$. Troubles may arise when $h_i^n = 0$ and $(3\theta - 1)(q_{i+1/2}^n - q_{i-1/2}^n) + (1 - \theta)(q_{i+3/2}^n - q_{i-3/2}^n) > 0$, because $h_i^{n+1} < 0$ everywhere in a small neighborhood of $\Delta t = 0$. These observations suggest a modification to the original algorithm where a limit depth value ε_h is defined and the cells with $h_i^n > \varepsilon_h$ are flagged as wet, while the cells with $h_i^n \leq \varepsilon_h$ are flagged as dry. The algorithm is described as follows.

At each time level t^n , the algorithm iteratively reduces the time step, in order to find the value $\Delta t = \Delta t_j$ (where Δt_j is the j -th guess) that satisfies the stability requirements and supplies positive depths h_i^{n+1} . At the beginning of the iterations, the initial guess $\Delta t = \Delta t_0$ is used, where the Eq. (40) is used for the calculation of Δt_0 . At the interfaces between the cells, the position $q_{i-1/2}^{n+1} = 0$ is made when $h_{i-1}^n < \varepsilon_h$ and $h_i^n < \varepsilon_h$, otherwise the Eq. (38) is used to calculate the discharge $q_{i-1/2}^{n+1}$ between the cells i and $i+1$. After this, the position $q_{i-1/2}^{n+1} = 0$ is made in the case that $q_{i-1/2}^{n+1} > 0$ and $h_{i-1}^n < \varepsilon_h$ or $q_{i-1/2}^{n+1} < 0$ and $h_i^n < \varepsilon_h$, because the flux must be limited in order to avoid the appearance of negative flow depth in dry cells. Finally, the flow depth in each cell is adjourned using Eq. (39). If $h_i^{n+1} < 0$ for some cell, the calculations are repeated with $\Delta t = \Delta t_j$, where $\Delta t_j = 0.7\Delta t_{j-1}$, and the process is iterated until $h_i^{n+1} \geq 0$ everywhere.

In the following, $\varepsilon_h = 10^{-9}$ m is used.

6.2.1 Riemann problems on flat bed

The modified q-centered scheme is applied to the two Riemann problems discussed in the preceding subsection, and the corresponding results are represented in Figure 11. The numerical solution of

the Riemann problem with $\mathbf{u}_L = (1.00 \ 5.00)^T$ and $\mathbf{u}_R = (0 \ 0)^T$ is represented in Figure 11a for the case $\Delta x = 0.02$. The inspection of the figure (solution at time $t = 5.001$ s) shows that there is no improvement of the numerical results with respect to the original *q-centered* scheme by de Almeida et al. (2012) for this problem. This enforces the conclusion that the error of the shock strength and position is due to the non-conservative nature of Eq. (38), and not to lack of mass conservation. In particular, the relative mass error is equal to $5.68 \cdot 10^{-16}$, which is very small as expected.

The results for the Riemann problem characterized by $\mathbf{u}_L = (1.00 \ -5.00)^T$ and $\mathbf{u}_R = (0 \ 0)^T$ are represented for the time $t = 5.002$ in Figure 11b. The inspection of the figure shows that the modified algorithm exhibits a backward moving shock which moves towards left with celerity equal to the flow velocity, violating the Rankine-Hugoniot theorem. The violation of the Rankine-Hugoniot condition is expected, since there is no exact solution for this Riemann problem. The relative difference between the computed final volume and the theoretical final volume is $2.70 \cdot 10^{-15}$, showing that the modified algorithm is successful in enforcing mass conservation with high accuracy.

6.2.2 Oscillations in the parabolic channel

The modified *q-centered* algorithm is applied with $\Delta x = 0.12$ m to the test by Thacker (1981), and the corresponding results are represented in Figure 12 for the times $t_1 = 350.24$ s (Figure 12a), $t_2 = 710.52$ s (Figure 12b), $t_3 = 1060.79$ s (Figure 12c), and $t_4 = 1421.02$ s (Figure 12d). The relative difference between the numerical and exact volume at time t_4 is $1.89 \cdot 10^{-10}$, showing a consistent improvement (nine orders of magnitude) with respect to the solution computed with the original *q-centred* scheme by de Almeida et al. (2012).

The comparison with the SWE exact results show that the new algorithm has improved capacity to capture the essentials of the solutions, namely the average slope of the free surface and the total mass. Nonetheless, the details of the representation remain unsatisfactory. For example,

from Figure 12a it is evident that the algorithm creates to the left of the channel a spurious receding wet-dry front that moves from left to right, and this is in contrast with the structure of the LInA equations, which admit only advancing or standing wet-dry fronts. The advancing front on the right of Figure 12a is represented with a shock, congruently with the structure of the LInA model, but this is in contrast with the front continuously connected to the bed that is supplied by the SWE exact solution. In addition, the position of the wetting front does not coincide with that supplied by the SWE. During the deceleration of the flow, the left receding shock of Figure 12a is transformed in a smoothly varying wave that is visible at the centre of Figure 12b. When this wave reaches the right wet-dry front, the free surface exhibits a peaked shape to the right of Figure 12c. Successively, this peaked free surface profile develops as a receding shock that moves towards left, and this shock is in turn broken into the smoothly varying wave that is visible at the centre of Figure 12d. Finally, the maximum flow depth computed is $h_{max} = 3.62$ m, and it is 13% greater than the exact value.

The reduction of the calculation time steps aiming at the satisfaction of a depth-positivity preserving property may lead to a consistent increment of the computational time. For the present case, the minimum time step is $\Delta t_{min} = 6.32 \cdot 10^{-11}$ s, and it is $2.04 \cdot 10^8$ times smaller than the minimum time step used by the original algorithm.

7 Discussion

The results presented in the preceding sections are discussed for their implications for flooding modelling with the LInA model. In particular, the differences between LInA and SWE are commented, and novel applicability limits are discussed.

7.1 Moving frontier modelling

A significant result found in Section 3 is that the drying of the wet bed is forbidden. In this case, the drying phenomenon may be substituted by a progressive reduction of the flow depth, which remains always greater than zero in the wetted points. This does not seem an issue in the case that the receding part of the flood is not important for the computation of the flooded areas extent, and for the computation of maximum flow depths and velocities. Nonetheless, there are cases where the flood wave is multi peaked, and this means that the recession curve following a peak may influence the dynamics of the flooding driven by the subsequent peak. How the LInA model influences the representation of the flooding dynamics generated by multiple peaked hydrographs is a question whose answer is still open. Nonetheless, it can be conjectured that the volume of water that is stuck on the flooded areas may reduce the flooding wave celerity. In addition, the volume of water stuck on the flooded areas is subtracted to the main flow, with the consequence that it is not available for successive flooding in the downstream areas. These observations should be the object of future confirm or rejection.

In the LInA model, the flooding phenomenon is characterized by an additional interesting feature found in Section 2, namely the presence of a shock at the wetting frontier. The speed of this shock is minor than the speed of the fastest signal in the SWE, as confirmed by the comparison in Section 3 between the solutions of the Riemann problem on dry bed supplied by LInA and SWE. The speed of the wetting front is commonly used to calibrate the floodplain roughness, and this implies that the slower front propagation speed should be compensated by lower values of the roughness (de Almeida and Bates 2013). Nonetheless, this could lead to an underestimation of the roughness in the flooded areas far from the wetting front. A roughness function depending on the Froude number and on the flow depth could be the optimal solution between the competing objectives of calibrating the roughness values that are valid in the main body of the flood and on the wetting front.

In order to ensure the physical representativeness of the flooding simulation, the limitation of the shock height at the wetting front is desirable. It is clear from Eqs. (12) and (13) that the flow

depth h_F and velocity u_F at the wetting front are linked by $|u_F| = \sqrt{gh_F/2}$, and this means that a control on the velocity of the wetting front could be used for rejection or acceptance of flooding simulation. For example, if the acceptable shock height at the wetting front is $h_{\text{lim}} = 0.05$ m, the limit velocity is $u_{\text{lim}} = 0.50$ m/s, and the simulations with $u_F > u_{\text{lim}}$ should be rejected. Lower values of the shock height at the wetting front could constitute a very strict requirement for the definition of the cases where the LInA model is acceptable for flooding simulations. Conversely, higher values of the shock height could relax this limit, but this could be unacceptable for the physical soundness of results.

The presence of a shock on the wetting front implies that numerical models written in non-conservative form should not be used for flooding propagation (Hou and LeFloch 1994), because they introduce an unavoidable error in the computation of shock speed and strength. This error could in turn adversely affect the roughness coefficient calibration. This has been confirmed in Section 6, where the performance of the *q-centered* scheme by de Almeida et al. (2012) has been verified with reference to the propagation on dry bed. For this reason, numerical models written in conservative form for the solution of the LInA are strongly recommended.

The numerical experiments of Section 6 have shown that a major source of numerical error in the original *q-centered* scheme is the lack of volume conservation in the cells where the wet bed dries. The modified algorithm proposed in Section 6 is based on two ingredients, namely the reduction of the time step and the flux limitation. The reduction of the time step is a standard procedure that enhances algorithms stability by avoiding that the flow depth becomes negative in wet cells (Burguete et al. 2007), and it has no influence on the structure of the problem solution. Conversely, the flux limitation, which is required to avoid that discharge flows out from dry cells, causes the formation of receding shocks that are forbidden by the LInA model mathematical structure and that violate the Rankine-Hugoniot condition. The modified algorithm introduces an additional adverse effect, namely the unacceptable increase of computational time caused by the

uncontrolled decrease of the time step. It is clear that an optimal algorithm should be based on the ability to preserve the depth-positivity under a reasonable time step limitation that is theoretically justified. Aiming at this, a procedure commonly used for the solution of SWE consists in adopting fully conservative finite volume schemes where the fluxes between the cells are calculated by means of special positivity-preserving Riemann solvers (Bouchut 2004, Cozzolino et al. 2012). Likely, a numerical scheme for the solution of LInA could be successfully based on this type of methodology.

7.2 Effects of uneven bed elevation and obstacles

In the Section 3, the impact of a wave against an obstacle has been studied. The corresponding analytic results show that the LInA model underestimates the flow depth at the obstacle, while the impact calms the flow down more rapidly than the SWE. The first consequence is that the flow velocity in the vicinity of obstacles may be underestimated, with consequences on the estimation of road infrastructures damaging (Kreibich et al. 2011) and pedestrian stability (Arrighi et al. 2017). Similarly, the underestimation of the flow depth may have consequences for the estimation of pedestrian stability (Arrighi et al. 2017), for the safety of transportation (Pregnolato et al. 2017), and for the evaluation of building damage (Pistrika et al. 2014). It is evident that these observations especially apply with reference to the evaluation of flooding damages and human safety in urban areas, where these aspects appear critical for the presence of numerous buildings and obstacles with complicate geometry.

Another consequence of flow depth underestimation at obstacles is that there are conditions in which the SWE exhibit sufficient energy to make the flow jump over the obstacle, while the LInA predicts full reflection (see the Riemann problem of Figure 6b). It is clear that the inaccurate treatment of obstacles may exclude large portions of land from the computation of the flooded areas, and that the flooded area error increases with the flooding duration.

The example Riemann problems in Section 6 show that the flow energy at bed elevation discontinuities is not conserved by the LInA model. In particular, energy is acquired at bed steps (positive bed elevation discontinuities) while energy is loss at bed drops (negative bed elevation discontinuities). In order to shed light on this fact, the conservation of energy for the LInA model is studied. Simple manipulations of Eq. (2) allow writing the following equation

$$(45) \quad \frac{\partial E_m(\mathbf{U})}{\partial t} + \frac{\partial}{\partial x} \left[ghu H(\mathbf{U}) \right] = u \frac{\partial h u^2}{\partial x} - ghu S_f,$$

which represents the balance equation for the mechanical energy $E_m(\mathbf{U}) = gh(h/2 + u^2/2 + z)$.

From Eq. (45) it is evident that the mechanical energy is not conserved, even in the case that friction is neglected, because the source term $u \partial h u^2 / \partial x$ is present. In particular, the local and total mechanical energy of the smooth flows is not conserved even in the case that the friction and the discharge through the boundaries are null. If the friction is negligible, the steady flow solution of Eq. (2) reduces to

$$(46) \quad \begin{aligned} \frac{\partial h u}{\partial x} &= 0 \\ \frac{\partial}{\partial x} H(\mathbf{U}) &= \frac{\partial}{\partial x} \frac{u^2}{2g} \end{aligned}$$

The Eq. (46) states that the head is not conserved through the domain, and this is in contrast with what is expected from physical intuition. After some algebraic manipulation, the integration of Eq. (46) between the abscissas x_1 and x_2 (with $x_1 < x_2$) leads to:

$$(47) \quad \frac{H(\mathbf{U}_1) - H(\mathbf{U}_2)}{h_1} = \frac{F^2(\mathbf{u}_1)}{2} \frac{\beta^2 - 2\beta}{(1-\beta)^2},$$

where $\mathbf{u}_i = (h_i \ h_i u_i)^T$ and $\mathbf{U}_i = (h_i \ h_i u_i \ z_i)^T$ are the vector of the conserved variables and the augmented vector of the conserved variables at the abscissa x_i ($i = 1, 2$), respectively, while $\beta = (z_2 - z_1)/h_l$ is the relative bed elevation variation.

This analysis confirms the results contained in Section 5 for the Riemann problem at bed steps and drops, because the Eq. (47) clarifies that head is gained if the bed slope is negative ($z_1 > z_2$), while head is lost in the case of positive bed slope ($z_1 < z_2$). The gain of energy with bed elevation variations is clearly in contrast with what is expected from physics, and this allows the introduction of a limit to acceptable Froude numbers, in order to save the physical soundness of results. For example, if the acceptable value for the spurious relative head variation is $(H(\mathbf{U}_1) - H(\mathbf{U}_2))/h_l = -0.1$, the Froude number $F(\mathbf{u}_1)$ must be smaller than 0.3 for $\beta = 0.45$.

The exact solutions contained in Section 5 have evidenced an additional result, namely the fact that there are initial conditions for which the Riemann problem at the bed drop has no solution. The inspection of Eq. (37) demonstrates that this issue is not related to an exotic class of initial conditions. In order to show this, it is sufficient to recall that the wetting fronts of the LInA model are shocks that move on the dry bed with Froude number equal to F_w . In this case, the position $F(\mathbf{u}_L) = F_w$ in Eq. (37) leads to the limit value $a/h_l = 1.56$ of the relative drop height. For example, with $h_F = 0.01$ m and $u_F = 0.22$ m/s, the maximum admissible drop height is $a_{max} = 0.016$ m. This result is particularly discouraging, because $a_{max} = 0.016$ m is far smaller than the height of the typical bed elevation irregularities that are found in flooding problems. In these circumstances, it is clear that the approximate solutions supplied by numerical models have no meaning, because the analytic solution of the flood propagation problem does not exist.

8 Conclusions

Despite the fact that the Local Inertia Approximation (LInA) has been applied for years in the field of flooding, the researchers have dedicated scarce efforts to finding exact solutions for this model. The study of moving wet-dry frontiers in the LInA model has shown that these are always characterized by a shock, and this justifies the general study of moving discontinuities. For this reason, the complete solution of the Riemann problem on horizontal frictionless bed has been tackled, demonstrating that receding shocks are forbidden. The consequence is that the drying of the wet bed is forbidden. In addition, the study of the nonbreaking wave on horizontal bed with friction has demonstrated that the formation of the shock at the wetting front is not confined to the frictionless case, but it is a completely general phenomenon for the LInA model.

Bed elevation discontinuities are common features of natural geometries and urban terrain configurations. The study of the Riemann problem with discontinuous bed elevation has demonstrated that the LInA model exhibits unphysical variation of energy at bed discontinuities, and that there are cases where the presence of a bed drop may cause the crisis of the mathematical model because no exact solution is possible. In addition, the absence of the momentum flux in the total thrust of the LInA equations may cause an underestimation of the flood stage and flooded areas when obstacles (bumps, levees, sidewalk steps, walls) are present. The analysis of steady solutions on smoothly variable bed have confirmed that the LInA model introduces spurious total head variations.

Following the preceding results, two new criteria for the definition of the applicability limits of the LInA model have been proposed. The first criterion is based on the velocity of the wetting front, and it is established in order to limit the height of the unphysical shock at the wet-dry frontier. The second criterion is based on the limitation of spurious energy variations through the domain.

In addition to these results, the numerical analyses have demonstrated that finite difference schemes written in non-conservative form are not able to capture the strength and the celerity of the wetting front, and that a modification to ensure the depth-positivity of the algorithm may lead to unfeasible reduction of the time step. Numerical algorithms written in conservative form should be

always preferred. Future research will be devoted to establishing a conservative numerical model with the depth-positivity property under a reasonable time step limitation.

Acknowledgments

Dr. Eng. Gabriella Petaccia is gratefully acknowledged for having supplied a postprint copy of the paper by Luigi Natale and Fabrizio Savi that is cited in the References list.

This research was partially funded by the University of Naples Parthenope through the funding program “Sostegno alla Ricerca Individuale 2015-2017” and “Ricerca competitiva triennio 2016-2018”.

Appendices

A. *Genuine non-linearity of the 1- and 2-waves in the system of Eq. (6)*

In the phase plane (h, hu) , the integral curves of the first characteristic field corresponding to the system of Eq. (6) are the solutions of the following ordinary differential equation (LeVeque 1992)

$$(A.1) \quad \frac{d\mathbf{u}}{ds} = \alpha(s) \mathbf{r}_1(\mathbf{u}(s)),$$

where $\alpha(s) \neq 0$ is a scaling factor. It is easy to see that the following is true along these curves:

$$(A.2) \quad \frac{d\lambda_1}{ds} = \nabla^T \lambda_1(\mathbf{u}(s)) \frac{d\mathbf{u}}{ds} = \alpha(s) \nabla^T \lambda_1(\mathbf{u}(s)) \mathbf{r}_1(\mathbf{u}(s)) = -\alpha(s) \frac{1}{2} \sqrt{\frac{g}{h}} \neq 0.$$

This implies that the first characteristic field is genuinely non-linear, because λ_l varies monotonically along the corresponding integral curves (LeVeque 1992). In a similar manner, it can be demonstrated that the second characteristic field is genuinely non-linear.

B. Rarefaction waves for the system of Eq. (6)

Eliminating $\alpha(s)ds$ from Eq. (A.1), the following

$$(B.1) \frac{d h}{1} = \frac{d h u}{-\sqrt{gh}}$$

is valid along the integral curves of the first characteristic field. The Eq. (B.1) can be solved with initial condition $\mathbf{u}(0) = \mathbf{u}_0$, supplying the explicit expression of the integral curve:

$$(B.2) hu + 2h\sqrt{gh}/3 = h_0 u_0 + 2h_0\sqrt{gh_0}/3.$$

The Eq. (B.2) is valid for $h > 0$, because the velocity u is infinite for $h = 0$. By definition (LeVeque 1992), the right state \mathbf{u} is connected to the left state \mathbf{u}_0 by a direct rarefaction wave contained into the first characteristic field if \mathbf{u} lies on the integral curve of Eq. (B.2), and the condition $\lambda_l(\mathbf{u}_0) < \lambda_l(\mathbf{u})$ is satisfied. It follows the definition

$$(B.3) R_l(\mathbf{u}, \mathbf{u}_0): 0 < h \leq h_0, \quad hu = h_0 u_0 + 2(h_0\sqrt{gh_0} - h\sqrt{gh})/3.$$

A similar reasoning, which is not reported here for the sake of brevity, shows that the right state \mathbf{u}_0 is connected to the left state \mathbf{u} by a backward rarefaction wave contained in the second

characteristic field if \mathbf{u} lies on the integral curve of the second characteristic field, and the condition $\lambda_2(\mathbf{u}) < \lambda_2(\mathbf{u}_0)$ is satisfied. It follows the definition

$$(B.4) \quad R_2^B(\mathbf{u}, \mathbf{u}_0): \quad 0 < h \leq h_0, \quad hu = h_0 u_0 - 2(h_0 \sqrt{gh_0} - h \sqrt{gh})/3.$$

C. Shock waves for the system of Eq. (6)

If the constant states \mathbf{u} and \mathbf{u}_0 are separated by a discontinuity that is propagating with speed σ , the Rankine-Hugoniot condition must be satisfied (LeVeque 1992). For the system of Eq. (6), this can be written as:

$$(C.1) \quad \begin{aligned} hu - h_0 u_0 &= \sigma(h - h_0) \\ \frac{gh^2}{2} - \frac{gh_0^2}{2} &= \sigma(hu - h_0 u_0). \end{aligned}$$

Some algebra shows that, for a given state \mathbf{u}_0 , the Hugoniot locus of the states \mathbf{u} that satisfy the Eq. (C.1) is represented in the phase plane (h, hu) by

$$(C.2) \quad hu = h_0 u_0 \pm (h - h_0) \sqrt{0.5g(h + h_0)},$$

with corresponding shock speed

$$(C.3) \quad \sigma = \pm \sqrt{0.5g(h + h_0)}.$$

In Eqs. (C.2)-(C.3), the sign minus and the sign plus define two distinct Hugoniot curves that are tangent to the eigenvectors $\mathbf{r}_1(\mathbf{u}_0)$ and $\mathbf{r}_2(\mathbf{u}_0)$, respectively. By definition (LeVeque 1992),

the right state \mathbf{u} is connected to left state \mathbf{u}_0 by a shock wave contained into the first characteristic field if \mathbf{u} lies on the Hugoniot curve tangent to $\mathbf{r}_1(\mathbf{u}_0)$, and the Lax condition $\lambda_1(\mathbf{u}_0) > \sigma > \lambda_1(\mathbf{u})$ is satisfied. It follows the definition

$$(C.4) \quad S_1(\mathbf{u}, \mathbf{u}_0): \quad h \geq h_0, \quad hu = h_0 u_0 + \sigma_1(\mathbf{u}, \mathbf{u}_0)(h - h_0), \quad \sigma_1(\mathbf{u}, \mathbf{u}_0) = -\sqrt{0.5g(h + h_0)}.$$

Similarly, the left state \mathbf{u} is connected to the right state \mathbf{u}_0 by a backward shock contained into the first characteristic field if \mathbf{u} lies on the Hugoniot curve tangent to $\mathbf{r}_2(\mathbf{u}_0)$, and the Lax condition $\lambda_2(\mathbf{u}) > \sigma > \lambda_2(\mathbf{u}_0)$ is satisfied. It follows the definition

$$(C.5) \quad S_2^B(\mathbf{u}, \mathbf{u}_0): \quad h \geq h_0, \quad hu = h_0 u_0 + \sigma_2(\mathbf{u}, \mathbf{u}_0)(h - h_0), \quad \sigma_2(\mathbf{u}, \mathbf{u}_0) = \sqrt{0.5g(h + h_0)}.$$

D. Monotonicity properties of the wave curves for the system of Eq. (6)

It is easy to demonstrate that the direct 1-wave curve H_1 of Eq. (9) is a continuous, strictly decreasing, and strictly concave function in the plane (h, hu) . In particular, it is possible to show that the first and the second derivative of hu with respect to h are negative on both the rarefaction and the shock part of the wave curve:

$$(D.1) \quad \begin{aligned} 0 < h < h_0, \quad \frac{dhu}{dh} &= -\sqrt{gh} < 0, \quad \frac{d^2hu}{dh^2} = -\frac{1}{2}\sqrt{\frac{g}{h}} < 0 \\ h > h_0, \quad \frac{dhu}{dh} &= -\frac{3gh + gh_0}{\sqrt{8g(h + h_0)}} < 0, \quad \frac{d^2hu}{dh^2} = -\frac{12g^2h + 20g^2h_0}{[8g(h + h_0)]^{3/2}} < 0 \end{aligned}$$

The continuity in h_0 of hu and of the corresponding derivatives follows immediately from the expressions of Eq. (9) and Eq. (D.1). Similarly, it is possible to show that the backward 2-wave H_2^B of Eq. (10) is a continuous, strictly increasing, and strictly convex function in the plane (h, hu) .

E. Contact discontinuities

The elimination of $\alpha(x)dx$ from Eq. (32) supplies

$$(E.1) \frac{d h}{1} = \frac{d z}{-1}, \quad d hu = 0,$$

which leads to the solution

$$(E.2) z + h = \text{const.}, \quad hu = \text{const.}$$

References

Abbott M.B. (1966) An introduction to the method of characteristics, Thames and Hudson, London.

Alcrudo F., Benkhaldoun F. (2001) Exact solutions to the Riemann problem of the shallow water equations with a bottom step, *Computers & Fluids* 30(6), 643-671. Doi: 10.1016/S0045-7930(01)00013-5.

Aldrigatti E., Zanolli P. (2005) A high resolution scheme for flows in open channels with arbitrary cross-section, *International Journal for Numerical Methods in Fluids* 47(8-9), 817-824. doi: 10.1002/fld.887.

Aronica T., Tucciarelli T., Nasello C. (1998) 2D Multilevel model for flood wave propagation in flood-affected areas, *ASCE Journal of Hydraulic Engineering* 124(4), 210-217. Doi: 10.1061/(ASCE)0733-9496(1998)124:4(210).

Arrighi C., Oumeraci H., Castelli F. (2017) Hydrodynamics of pedestrians' instability in floodwaters, 21(1) 515-531. Doi: 10.5194/hess-21-515-2017.

Bates P.D., Horritt M.S., Fewtrell T.J. (2010) A simple inertial formulation of the shallow water equations for efficient two-dimensional flood inundation modelling, *Journal of Hydrology*, 387(1-2), 33-45. Doi: 10.1016/j.jhydrol.2010.03.027.

Bouchut, F. (2004) Nonlinear stability of finite volume methods for hyperbolic conservation laws, Birkhäuser, Basel.

Burguete J., García-Navarro P., Murillo J., García-Palacín I. (2007) Analysis of the friction term in the one-dimensional Shallow-water model, *ASCE Journal of Hydraulic Engineering* 133(9), 1048-1063. Doi: 10.1061/(ASCE)0733-9429(2007)133:9(1048).

Chen Y., Zhou H., Zhang H., Du G., Zhou J. (2015) Urban flood risk warning under rapid urbanization, *Environmental Research* 139, 3-10. Doi: 10.1016/j.envres.2015.02.028.

Coulthard T.J., Neal J.C., Bates P.D., Ramirez J., de Almeida G.A.M., Hancock G.R. (2013) Integrating the LISFLOOD-FP 2D hydrodynamic model with the CAESAR model: implication for modelling landscape and evolution, *Earth Surface Processes and Landforms* 38(15), 1897-1906. Doi: 10.1002/esp.3478.

Cozzolino L., Della Morte R., Covelli C., Del Giudice G., Pianese D. (2011) Numerical solution of the discontinuous-bottom Shallow-water Equations with hydrostatic pressure distribution at the step, *Advances in Water Resources* 34(11), 1413-1426. Doi: 10.1016/j.advwatres.2011.07.009.

Cozzolino L., Della Morte R., Del Giudice G., Palumbo A., Pianese D. (2012) A well-balanced spectral volume scheme with the wetting–drying property for the shallow-water equations, *Journal of Hydroinformatics* 14(3), 745–760. Doi: 10.2166/hydro.2012.035.

Cozzolino L., Pepe V., Morlando F., Cimorelli L., D'Aniello A., Pianese D. (2017) Exact solution of the dam-break problem for constrictions and obstructions in constant width rectangular

channels, ASCE Journal of Hydraulic Engineering 143(11), 04017047. doi: 10.1061/(ASCE)HY.1943-7900.0001368.

de Almeida G.A.M., Bates P. (2013) Applicability of the local inertial approximation of the shallow water equations to flood modeling, Water Resources Research 49(8), 4833-4844. Doi: 10.1002/wrcr.20366.

de Almeida G.A.M., Bates P., Freer J.E., Souvignet M. (2012) Improving the stability of a simple formulation of the shallow water equations for 2-D flood modeling, Water Resources Research 48(5), W05528. Doi: 10.1029/2011WR011570.

Doocy S., Daniels A., Murray S., Kirsch T.D. (2013) The Human Impact of Floods: a Historical Review of Events 1980-2009 and Systematic Literature Review, PLOS Current disasters. Doi: 10.1371/currents.dis.f4deb457904936b07c09daa98ee8171a.

Dottori F., Todini E. (2011) Developments of a flood inundation model based on the cellular automata approach: Testing different methods to improve model performance, Physics and Chemistry of the Earth 36(7-8), 266-280. Doi: 10.1016/j.pce.2011.02.004.

Falter D., Vorogushyn S., Lhomme J., Apel H., Gouldby B., Merz B. (2013) Hydraulic model evaluation for large-scale flood risk assessments, Hydrological Processes 27(9), 1331-1340. Doi: 10.1002/hyp.9553.

Galbiati G., Savi F. B. (1995) Evaluation of the comparative influence of soil hydraulic properties and roughness on overland flow at the local scale, Journal of Agriculture Engineering Research 61(3), 183-190. Doi: 10.1006/jaer.1995.1045.

Hou T.Y., LeFloch P.G. (1994) Why nonconservative schemes converge to wrong solutions: error analysis, Mathematics of Computation 62, 497-530. Doi: 10.1090/S0025-5718-1994-1201068-0.

Hunter N.H., Horritt M.S., Bates P.D., Wilson M.D., Werner M.G.F. (2005) An adaptive time step solution for raster-based storage cell modelling of floodplain inundation, Advances in Water Resources 28(9), 975-991. Doi: 10.1016/j.advwatres.2005.03.007.

Kreibich H., Piroth K., Seifert I., Maiwald H., Kunert U., Schwarz J., Merz B., Thielen A.H. (2009) Is flow velocity a significant parameter in flood damage modelling?, *Natural Hazard and Earth System Sciences* 9(5), 1679-1692. Doi: 10.5194/nhess-9-1679-2009.

Kundzewicz Z.W., Kanae S., Seneviratne S.I., Handmer J., Nicholls N., Peduzzi P., Mechler R., Bouwer L.M., Arnell N., Mach K., Muir-Wood R., Brakenridge G.R., Kron W., Benito G., Honda Y., Takahashi K., Sherstyukov B. (2014) Flood risk and climate change: global and regional perspectives, *Hydrological Sciences Journal* 59(1), 1-28. Doi: 10.1080/02626667.2013.857411.

LeFloch P.G., Thanh M.D. (2007) The Riemann problem for the shallow water equations with discontinuous topography, *Communications in Mathematical Sciences* 5(4), 865-885. <https://projecteuclid.org/euclid.cms/1199377555>.

LeVeque R.J. (1992) Numerical methods for conservation laws, Birkhäuser, Basel.

LeVeque R.J., George D.L., Berger M.J. (2011) Tsunami modelling with adaptively refined finite volume methods, *Acta Numerica* 20, 2011-289. Doi: 10.1017/S0962492911000043.

Liang Q., Du G., Hall J.W., Borthwick A.G.L. (2008) Flood inundation modeling with an adaptive Quadtree Grid Shallow water Equation solver, *ASCE Journal of Hydraulic Engineering* 134(11), 1603-1610. Doi: 10.1061/(ASCE)0733-9429(2008)134:11(1603).

Martins R., Leandro J., Djordjević S. (2015) A well balanced Roe scheme for the local inertial equations with an unstructured mesh, *Advances in Water Resources* 83, 351-363. Doi: 10.1016/j.advwatres.2015.07.007.

Martins R., Leandro J., Djordjević S. (2016a) Analytical and numerical solutions of the Local Inertial Equations, *International Journal of Non-Linear Mechanics* 81, 222-229. Doi: 10.1016/j.ijnonlinmec.2016.01.015.

Martins R., Leandro J., Djordjević S. (2016b) Analytical solution of the classical dam-break problem for the Gravity Wave-Model equations, *Journal of Hydraulic Engineering* 142(5), 06016003. Doi: 10.1061/(ASCE)HY.1943-7900.0001121.

Martins R., Leandro J., Djordjević S. (2016c) Influence of sewer network models on urban flood damage assessment based on coupled 1D/2D models, *Journal of Flood Risk Management* (in press). Doi: 10.1111/jfr3.12244.

Martins R., Leandro J., Chen A.S., Djordjević S. (2017) A comparison of three dual drainage models: shallow water vs Local Inertial vs Diffusive Wave, *Journal of Hydroinformatics* 19(3), 331-348. Doi: 10.2166/hydro.2017.075.

Martins R., Leandro J., Chen A.S., Djordjević S. (2018) Wetting and drying numerical treatments for the Roe Riemann scheme, *Journal of Hydraulic Research* 56(2), 256-267. Doi: 10.1080/00221686.2017.1289256.

Mateo C.M.R., Yamazaki D., Kim H., Champathong A., Vaze J., Oki T. (2017) Impacts of spatial resolution and representation of flow connectivity on large-scale simulation of floods, *Hydrology and Earth System Sciences* 21(10), 5143-5163. Doi: 10.5194/hess-21-5143-2017.

Mignot E., Paquier A., Haider S. (2006) Modelling floods in a dense urban area using 2D shallow water equations, *Journal of Hydrology* 327(1-2), 186-199. Doi: 10.1016/j.jhydrol.2005.11.026.

Montuori C., Greco V. (1973) Fenomeni di moto vario a valle di una paratoia piana, *L'Energia Elettrica* 50(2), 73-88 (in Italian).

Moramarco T., Melone F., Singh V.P. (2005) Assessment of flooding in urbanized ungauged basins: a case study in the Upper Tiber area, Italy, *Hydrologic Processes* 19(10), 1909-1924. Doi: 10.1002/hyp.5634.

Natale L., Savi F. (1991), Espansione di onde di sommersione su terreno inizialmente asciutto, *Idrotecnica* 1991(6), 397-406. (in Italian)

Neal J., Schumann G., Fewtrell T., Budimir M., Bates P., Mason D. (2011) Evaluating a new LISFLOOD-FP formulation with data from the summer 2007 floods in Tewkesbury, UK, *Journal of Flood Risk Management* 4(2), 88-95. Doi: 10.1111/j.1753-318X.2011.01093.x.

Neal J., Villanueva I., Wright N., Willis T., Fewtrell T., Bates P. (2012) How much physical complexity is needed to model flood inundation?, *Hydrological Processes* 26(15), 2264-2282. Doi: 10.1002/hyp.8339.

Nguyen N.Y., Ichikawa Y., Ishidaira H. (2016) Estimation of inundation depth using flood extent information and hydrodynamic simulations. *Hydrological Research letters* 10(1), 39-44. Doi: 10.3178/hrl.10.39.

Pistrika A., Tsakiris G., Nalbantis I. (2014) Flood depth-damage functions for built environment, *Environmental Processes* 1(4), 533-572. Doi: 10.1007/s40710-014-0038-2.

Pregnolato M., Ford A., Wilkinson S.M., Dawson R.J. (2017) The impact of flooding on road transport: A depth-disruption function, *Transportation Research Part D: Transport and Environment* 55, 67-81. Doi: 10.1016/j.trd.2017.06.020.

Savage J.T.S., Pianosi F., Bates P., Freer J., Wagener T. (2016) Quantifying the importance of spatial resolution and other factors through global sensitivity analysis of a flood inundation model, *Water Resources Research* 52(11), 9146-9163. Doi: 10.1002/2015WR018198.

Sielecki A. (1968) An energy-conserving difference scheme for the storm surge equations, *Monthly Weather Review*, 1968, 96(3), 150-156. Doi: 10.1175/1520-0493(1968)096<0150:AECDSE>2.0.CO;2.

Sobey R.J. (2009) Wetting and drying in coastal flows, *Coastal Engineering* 56(5-6), 565-576. Doi: 10.1016/j.coastaleng.2008.12.001.

Thacker W.C. (1981) Some exact solutions to the nonlinear shallow-water wave equations, *Journal of Fluid Mechanics* 107, 499-508. Doi: 10.1017/S0022112081001882.

Toro E.F. (2001) Shock-capturing methods for free-surface flows, Wiley, Chichester, UK.

Uusitalo S. (1960) The numerical calculation of wind effect on sea level elevations, *Tellus*, 1960, 12(4), 427-435. Doi: 10.1111/j.2153-3490.1960.tb01329.x.

Wang Y., Liang Q., Kesserwani G., Hall J.W. (2011) A 2D shallow flow model for practical dam-break simulations, IAHR Journal of Hydraulic Research 49(3), 307-316. Doi: 10.1080/00221686.2011.566248.

Xing Y., Shu C.-W. (2005) High order finite difference WENO schemes with the exact conservation property for the shallow water equations, Journal of Computational Physics 2018(1), 206-227. doi: 10.1016/j.jcp.2005.02.006.

Yamazaki D., de Almeida G.A.M., Bates P. (2013) Improving computational efficiency in global river models by implementing the local inertial flow equation and a vector-based river network map, Water Resources Research 49(11), 7221-7235. Doi: 10.1002/wrcr.20552.

Yamazaki D., Tanaka T., Bates P. (2015) Rapid and stable flood inundation modelling using the Local Inertial Equation, Journal of the Japan Society of Hydrology and Water Resources 28(3), 124-130. Doi: 10.3178/jjshwr.28.124. (in Japanese)

Table 1. Riemann problem on horizontal bed. Initial data for the example solutions in Figure 1.

Configuration	h_L (m)	u_L (m/s)	h_R (m)	u_R (m/s)
No solution (Fig. 1a)	0.50	1.00	0.50	5
Rarefaction – rarefaction (Fig. 1b)	1	1	1	3
Shock – rarefaction (Fig. 1c)	1	3	2	1.5
Shock – shock (Fig. 1d)	1	3	1	1

Table 2. Riemann problem at the dry bed step. Initial data for the example solutions in Figure 6.

Example solution	h_L (m)	u_L (m/s)	z_L (m/s)	h_R (m)	u_R (m/s)	z_R (m/s)
Figure 5a	1.00	0.20	0	0	0	0.50
Figure 5b	1.00	1.50	0	0	0	1.45
Figure 5c	1.00	5.00	0	0	0	0.50
Figure 5d	1.00	5.00	0	0	0	0.10

Table 3. Riemann problem at the dry bed drop. Initial data for the example solutions in Figure 7.

Example solution	h_L (m)	u_L (m/s)	z_L (m/s)	h_R (m)	u_R (m/s)	z_R (m/s)
Figure 6a	1.00	0.20	0	0	0	-0.20
Figure 6b	1.00	0.20	0	0	0	-1.01
Figure 6c	0.18	1.11	0	0	0	-0.01
Figure 6d	1.00	5.00	0	0	0	-1

Figure 1. Riemann problem on horizontal bed. Graphical solutions for the initial data in Table 1.

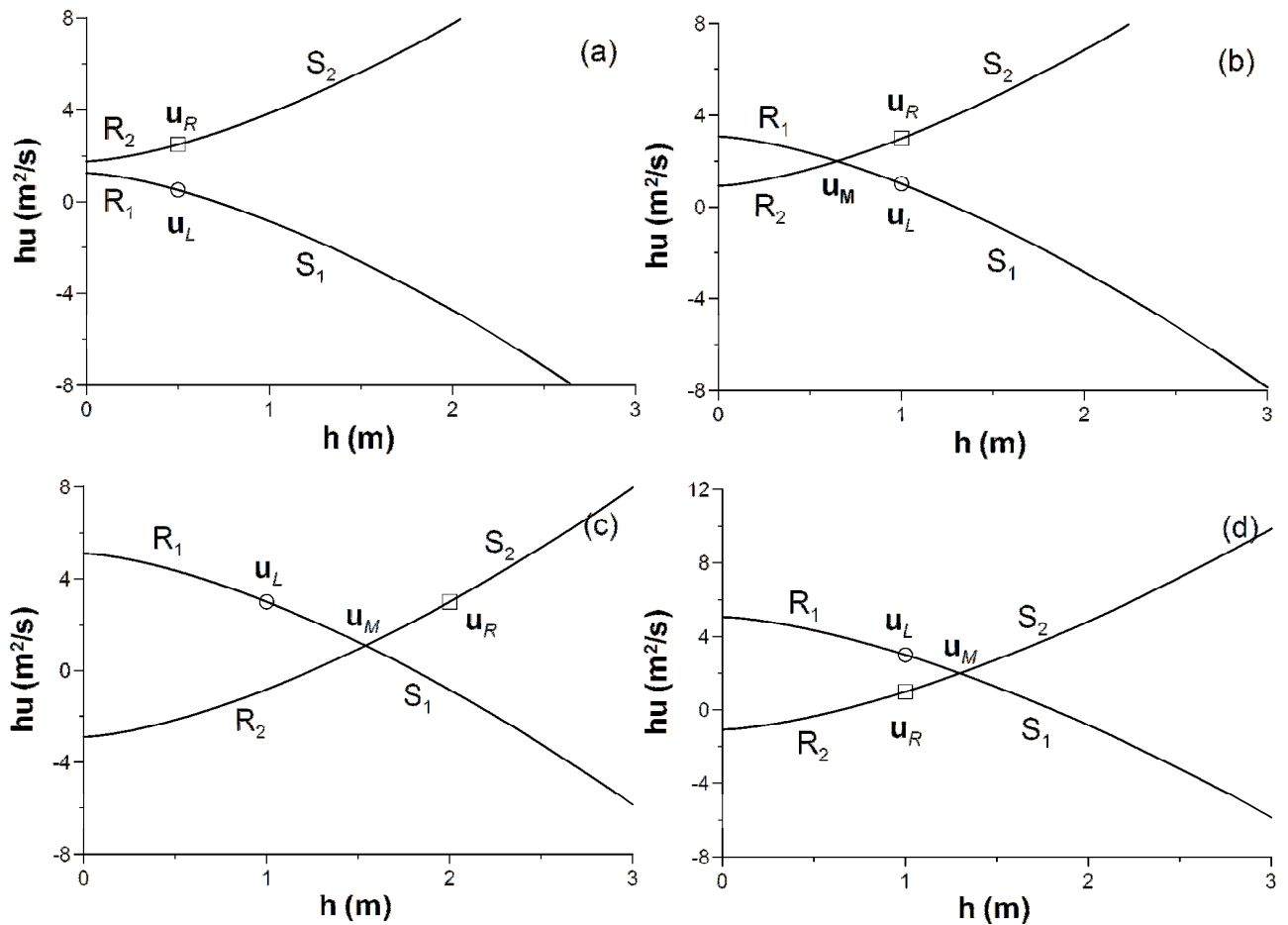


Figure 2. Riemann problem on horizontal dry bed. Exact solution at $t = 5$ s (flow depth).

Rarefaction-shock with $h_L = 1$ m, $h_{LU} = 0.20$ m²/s (a); shock-shock with $h_L = 1$ m, $h_{LU} = 5$ m²/s (b).

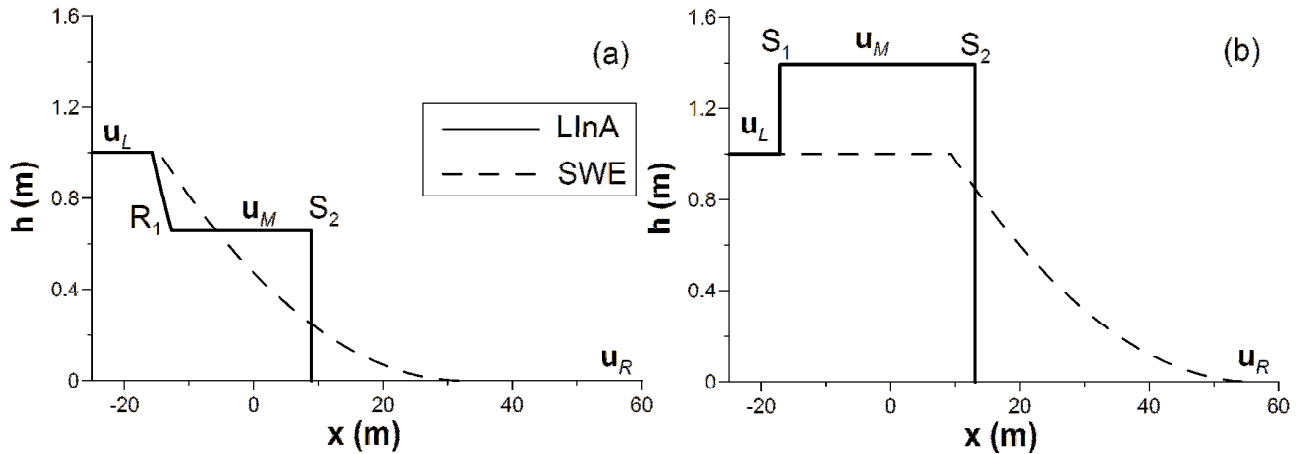


Figure 3. Riemann problem on horizontal dry bed. Comparison of the wave speeds.

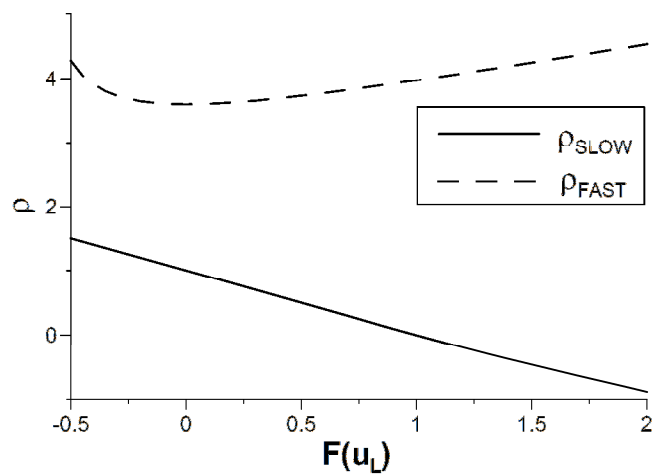


Figure 4. Impact on a wall. Exact solution at $t = 5$ s (flow depth) for $h_L = 1$ m and $h_L u_L = 1.5$ m²/s (a); ratio $h_{\text{LInA}}/h_{\text{SWE}}$ at the wall for different values of $F(u_L)$ (b).

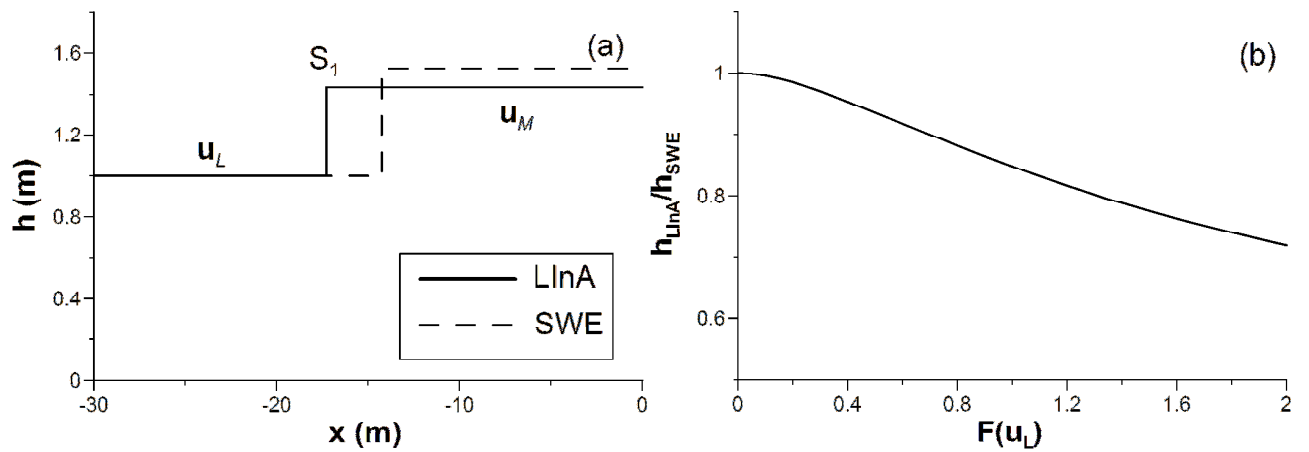


Figure 5. Wetting of the horizontal floodplain.

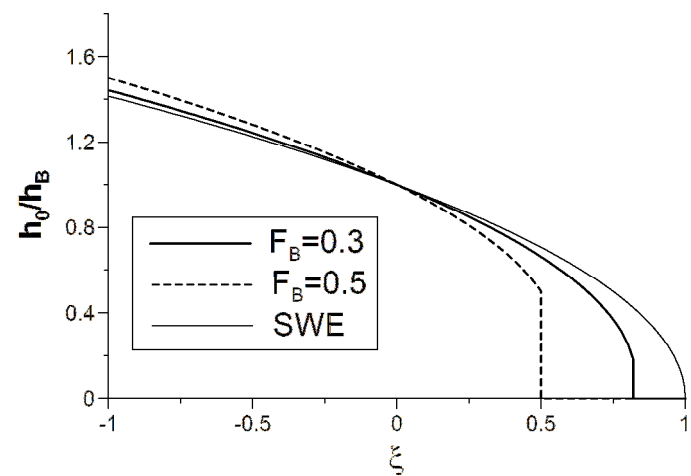


Figure 6. Riemann problem at the dry bed step. Exact solution at $t = 5$ s (free surface elevation) for the initial data in Table 2.

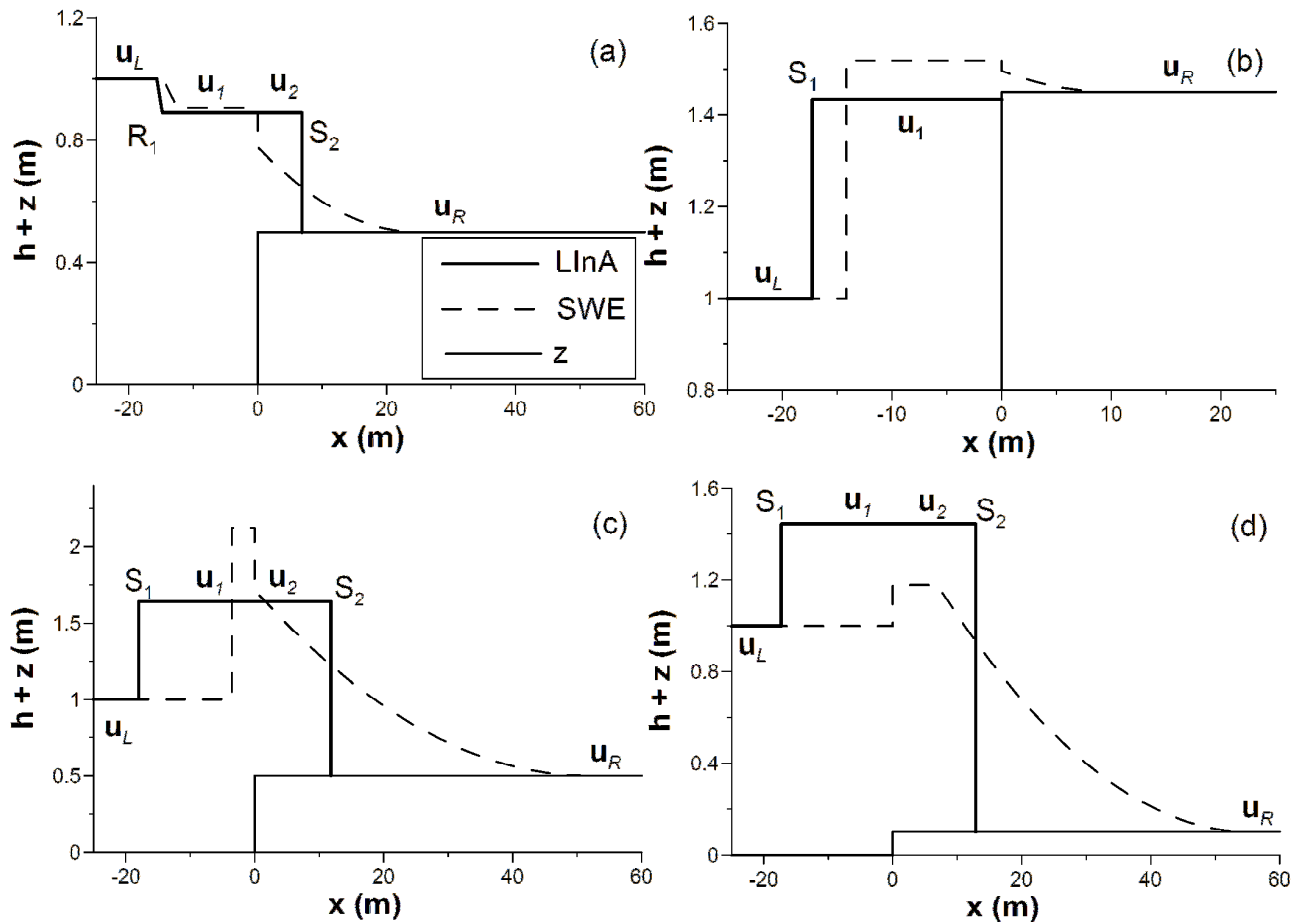


Figure 7. Riemann problem at the dry bed drop. Exact solution at $t = 5$ s (free surface elevation) for the initial data in Table 3.

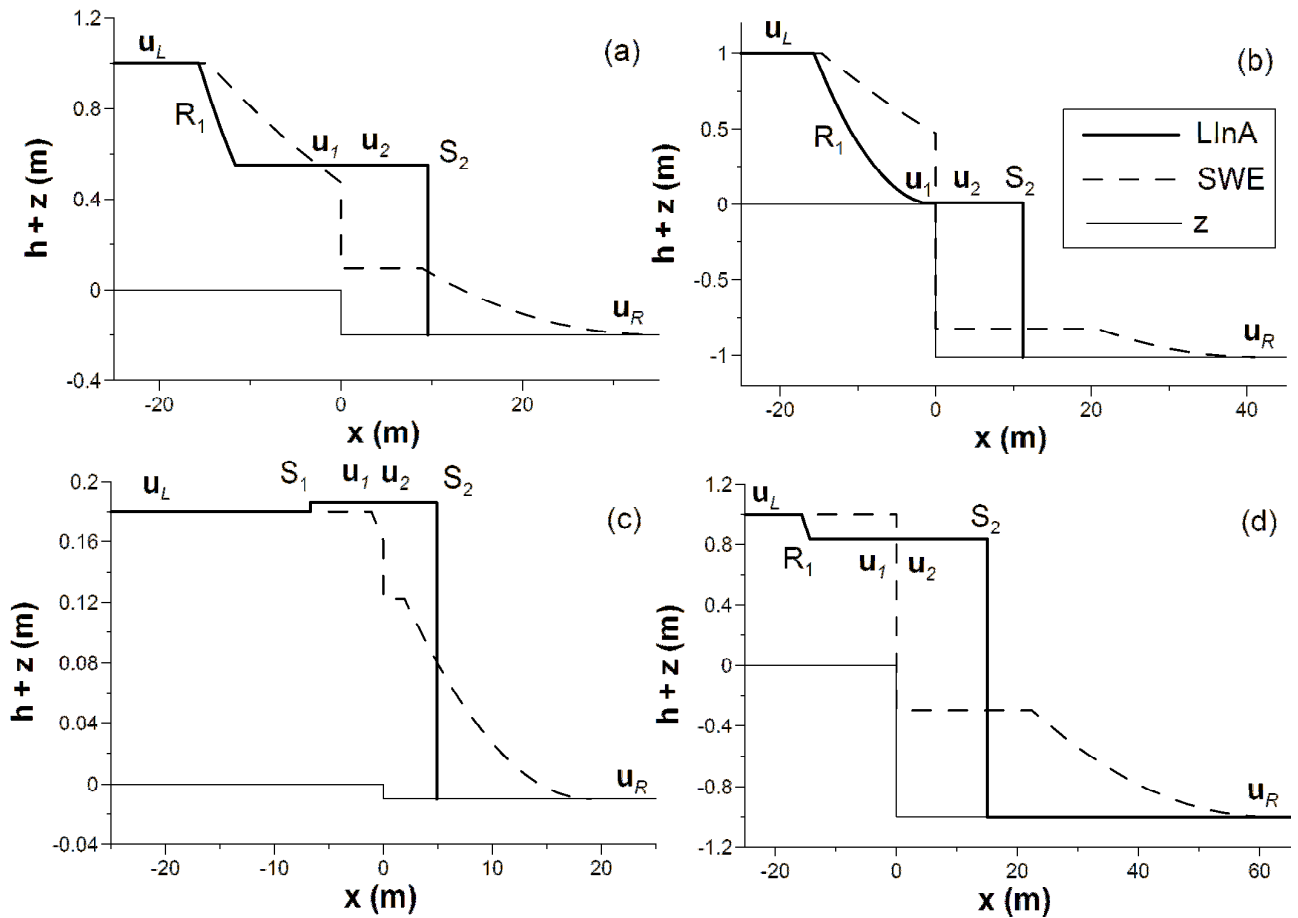


Figure 8. Limits of existence for the Riemann problem at the bed drop.

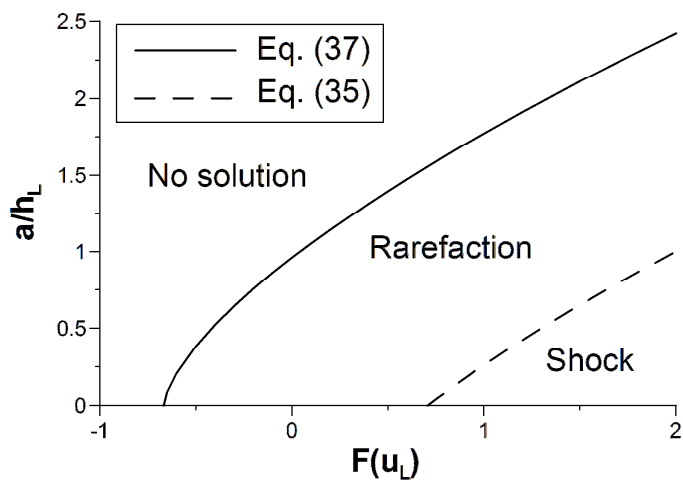


Figure 9. Finite-difference q-centered scheme by de Almeida et al. (2012). Flow depth at time $t = 5.002$ s of the Riemann problem on horizontal dry bed with $h_L = 1$ m and $u_L = 5$ m/s (a), and with $h_L = 1$ m and $u_L = -5$ m/s (b).

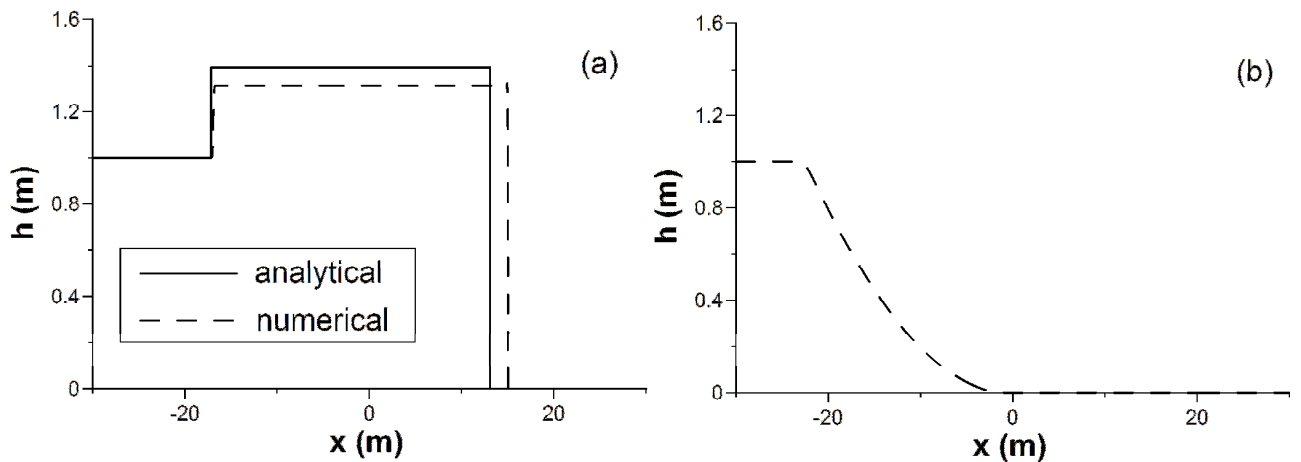


Figure 10. Finite-difference q-centered scheme by de Almeida et al. (2012). Free surface elevation for the oscillating channel at times $t_1 = 350.17$ s (a), $t_2 = 710.39$ s (b), $t_3 = 1060.57$ s (c), and $t_4 = 1420.73$ s (d).

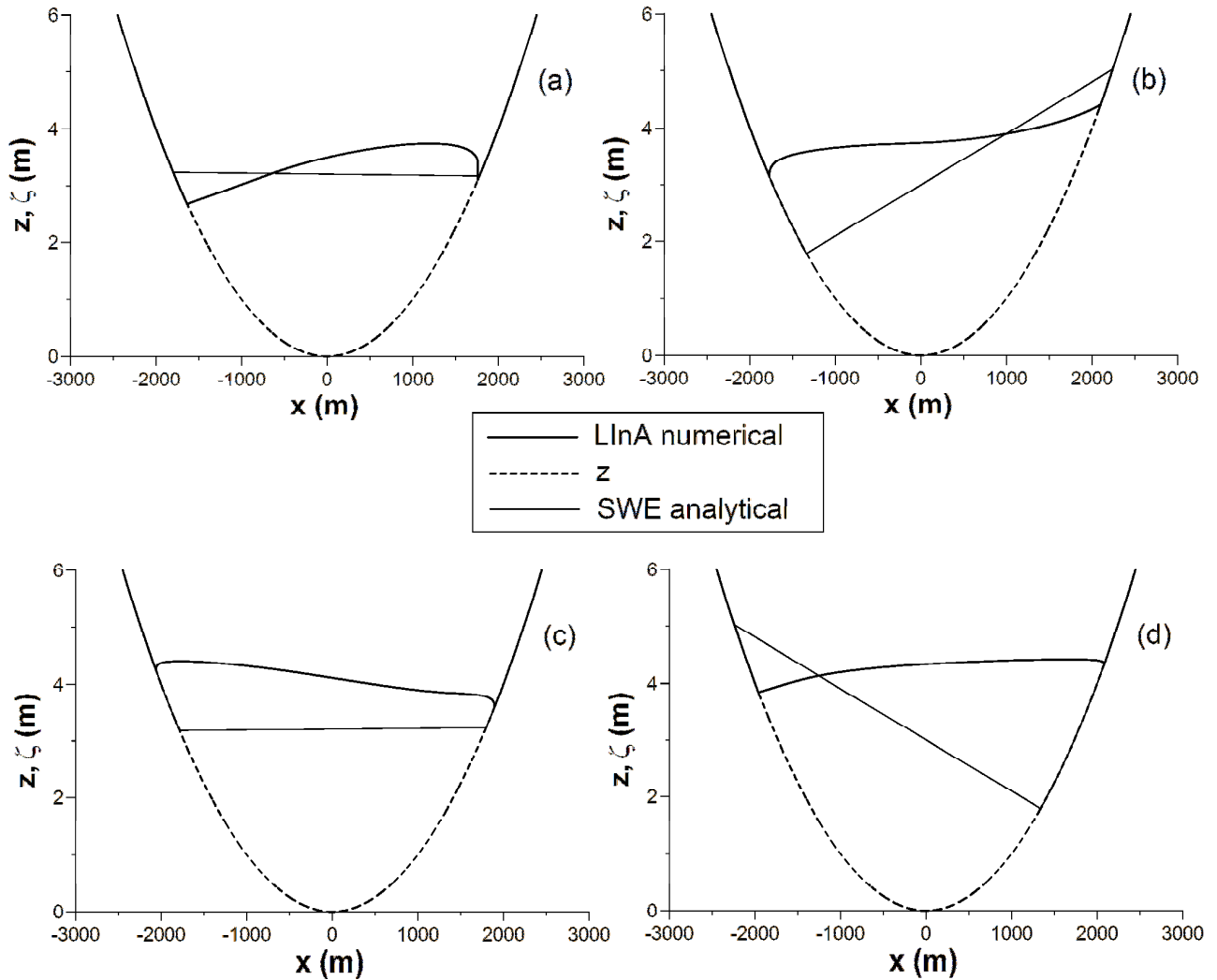


Figure 11. Modified finite-difference q-centered scheme. Flow depth of the Riemann problem on horizontal dry bed with $h_L = 1$ m and $u_L = 5$ m/s at time $t = 5.001$ s (a), and with $h_L = 1$ m and $u_L = -5$ m/s at time 5.002 (b).

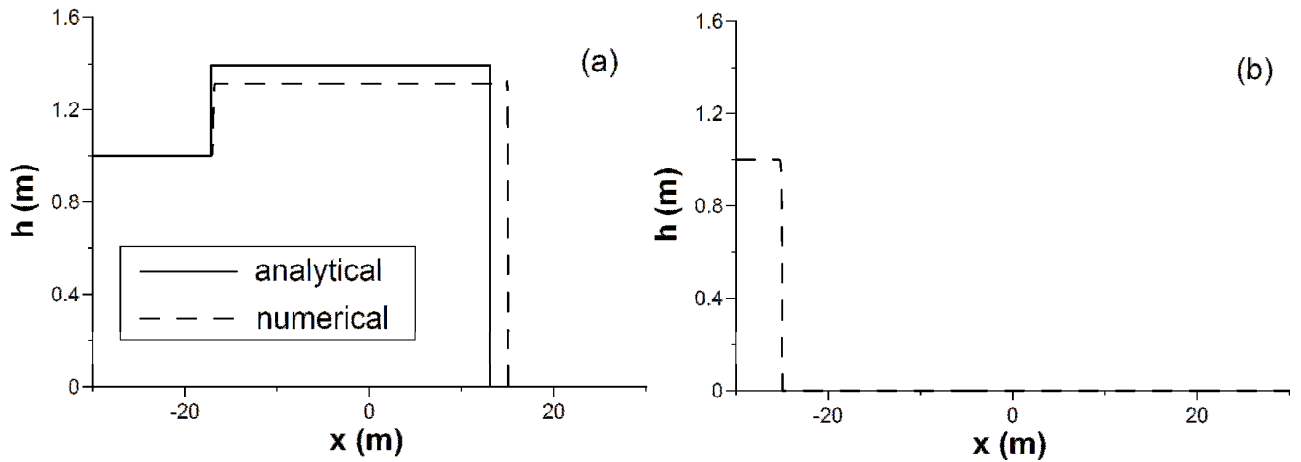


Figure 12. Modified finite-difference q-centered scheme. Free surface elevation for the oscillating channel at times $t_1 = 350.24$ s (a), $t_2 = 710.52$ s (b), $t_3 = 1060.79$ s (c), and $t_4 = 1421.02$ s (d).

